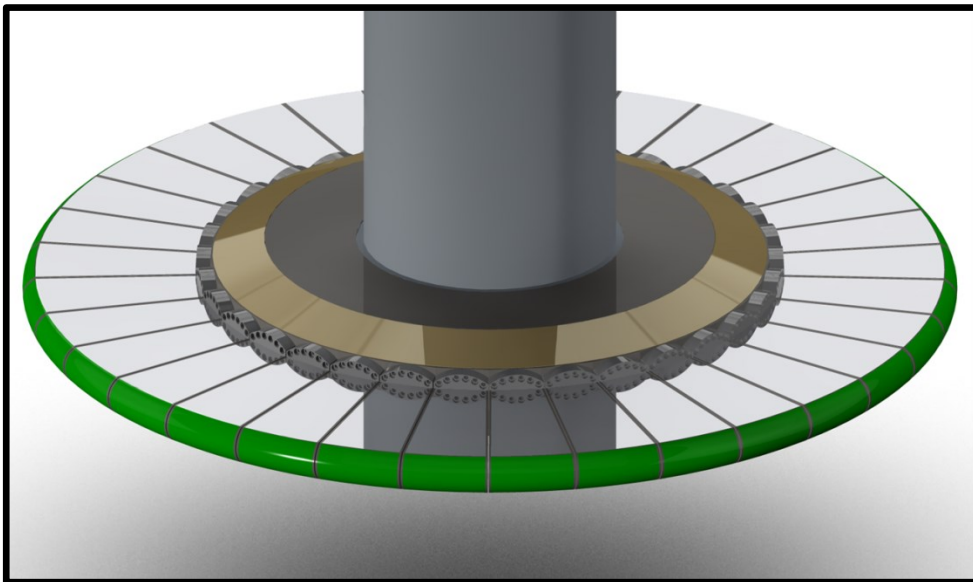


# A design study on the ESS spallation target and design considerations on the helium circulator

September 2014

O. Caretta, T. Davenne, J. O'Dell, C.J. Densham  
STFC Rutherford Appleton Laboratory, Didcot, OX11 0QX, UK



This report presents the results of a study carried out on the target of the European Spallation Source (ESS) by the High Power Targets Group at Rutherford Appleton laboratory over 2012 - 2014 under contract to ESS. The work focused on the design and thermo-mechanical analysis of the spallation target subjected to a 2.5 GeV, 5MW proton beam.

Section 1 reports a study on the initial tungsten “stacked plates” baseline design which estimates temperature jumps in the plates resulting in high thermal stresses of the order of 340MPa.

Section 2 proposes a design study of the target where segmentation of the tungsten plates is used as a mean to reduce the thermal mechanical stresses in the target material. A modular-type functional design of the target is then presented which offers increased ease of manufacturing, higher reliability and the possibility to perform remote maintenance of the target wheel.

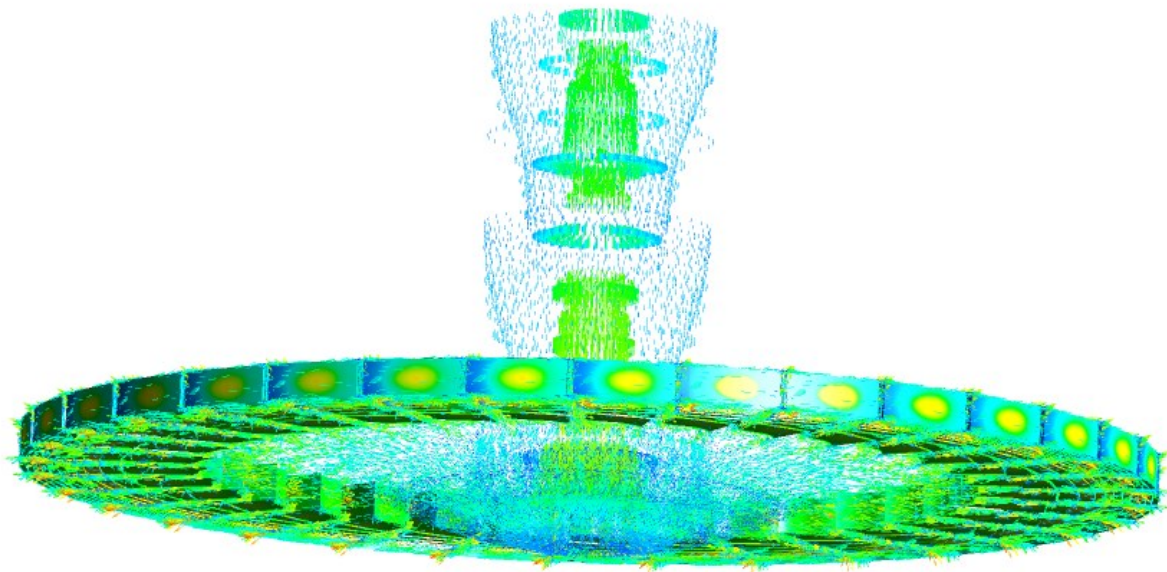
Finally Section 3 presents some design considerations on a helium circulator capable of delivering the 3kg/s mass flow rate required for the cooling of the target.

## Contents

1	Model of the baseline design .....	3
1.1	Thermal model .....	3
1.2	Stress Model.....	11
1.3	Discussion.....	14
2	A “sunflower” packed bed target design for ESS .....	16
2.1	Design of a granular target and supporting structure .....	17
2.2	Thermal mechanical model of the beam heat signature.....	24
2.3	Fluid mechanical steady state combined model .....	27
2.4	Thermal mechanical “steady state” .....	31
2.5	Discussion.....	33
2.6	Modular design .....	34
3	Helium gas circulation energy considerations .....	39
3.1	A multistage centrifugal fan type compressor.....	40
3.2	A closed cycle brayton cycle .....	42
4	Appendices .....	43
4.1	Appendix: Predicted performance of Dresser multistage centrifugal compressor .....	43
4.2	Appendix 1 Tungsten material properties .....	48
4.3	Appendix: tungsten yield strength data as published by Plansee .....	49
4.4	Appendix: sensitivity of the thermal analysis to grains swelling .....	50
5	References.....	53

## 1 Model of the baseline design

The starting point of the study was the target baseline for the proposed ESS facility comprising a helium cooled wheel of tungsten segments [1]. Each one of the 33 sectors composing the target wheel is made up by an array of tungsten plates which essentially constitutes a target of its own, drawing and returning coolant from a common manifold. Such an arrangement distributes the residual activity over a large volume of target and so it is thought to be safer and not to require active cooling in a power failure scenario.



### 1.1 Thermal model

A CFD model of a single segment of the baseline design geometry (courtesy of Chen Yuming) has been run in order to obtain the steady state helium flow field within the target wheel. The geometry (Figure 1) includes the shaft with inlet and outlet channels as well as the detail of the 12 separate tungsten slabs and the helium channels between them.

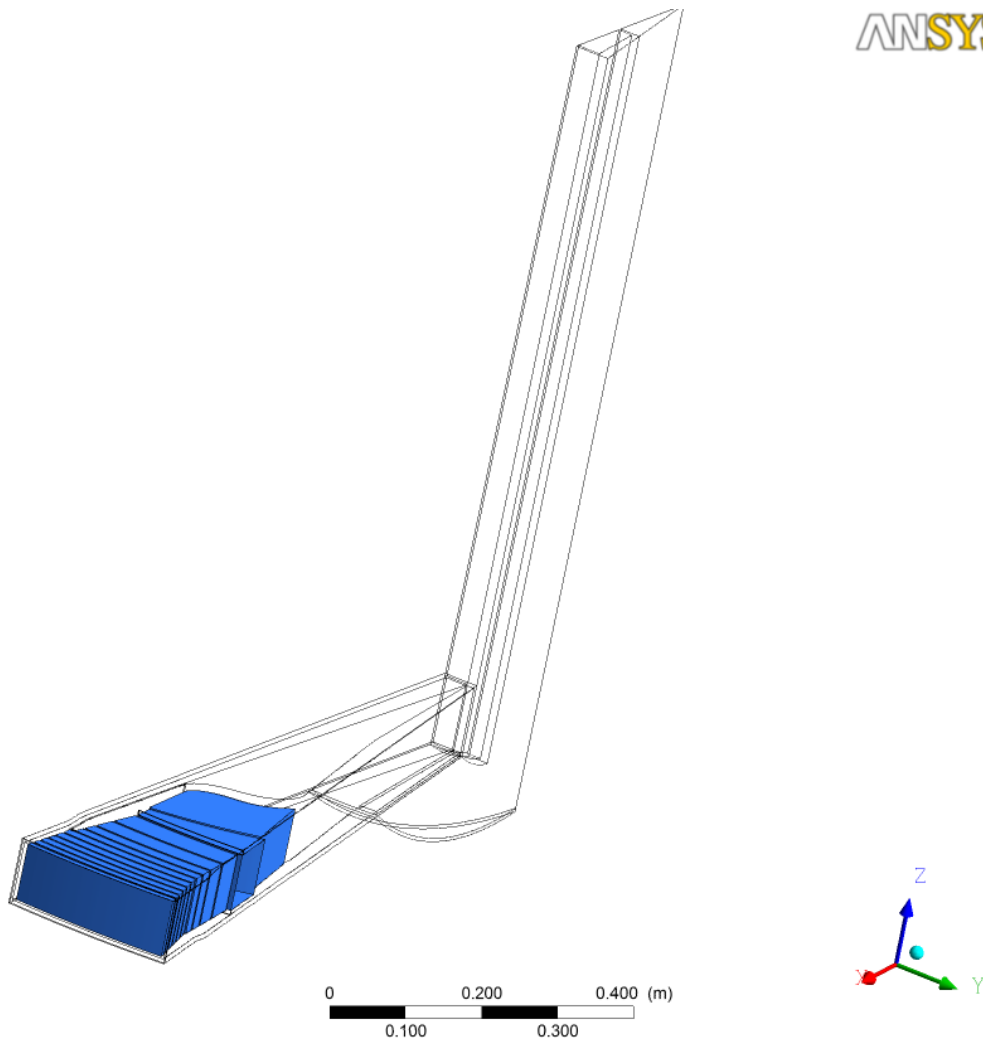


Figure 1 CFD Geometry

The mass flow rate in the single segment is based on a total mass flow of 3kg/s equally divided among the segments. The discharge pressure is assumed to be 3bar absolute. The result shows a pressure rise in the helium of 0.6bar (Figure 2).

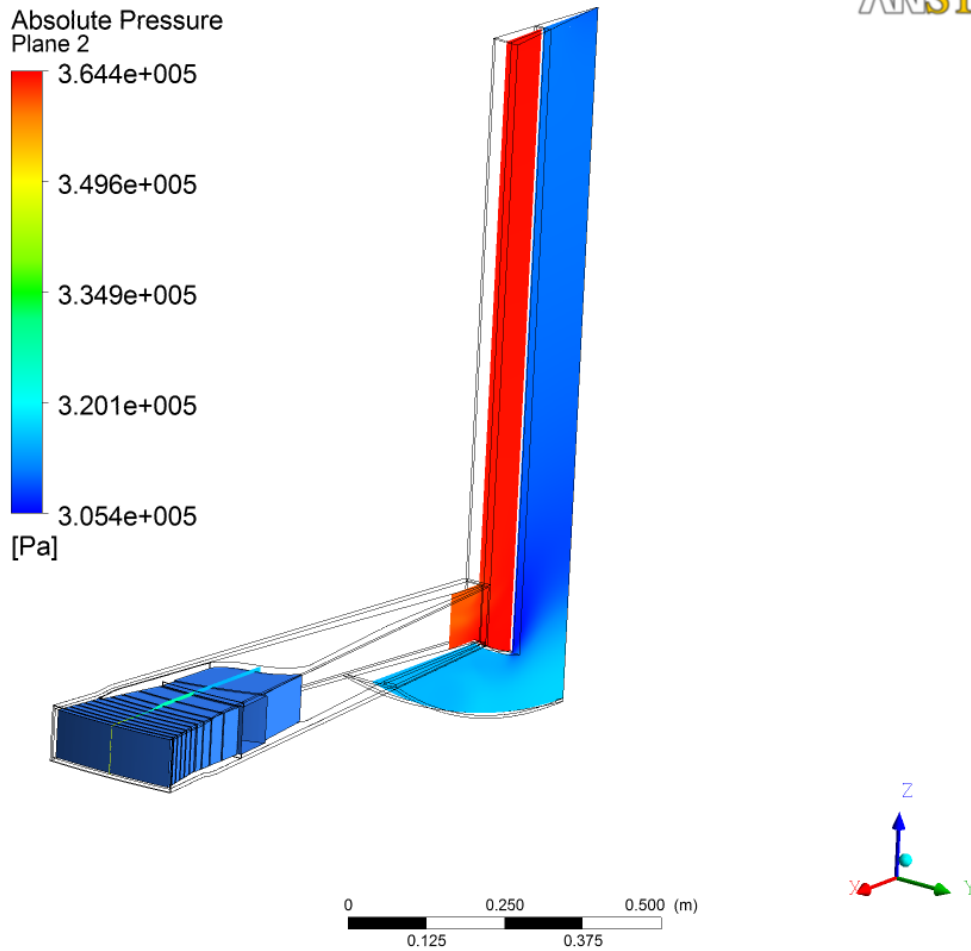


Figure 2 Pressure drop through wheel

The peak helium velocity is calculated as 369m/s and the peak Mach number is 0.356. The peak heat flux at the surface of the tungsten slabs for this steady state model is 1.2MW/m<sup>2</sup>. This is about half of the peak heat flux achieved in the ISIS TS1 Water cooled target running at nominal conditions. The helium temperature increases by 200°C which is simply a function of the total heat load in the target (around 3MW) and the mass flow. Very little flow was passing between slab 6 and 7 (Figure 3) with the design geometry modelled resulting in one surface with a very low heat transfer coefficient (Figure 4). This issue has since been remedied by adding an additional flow guide.

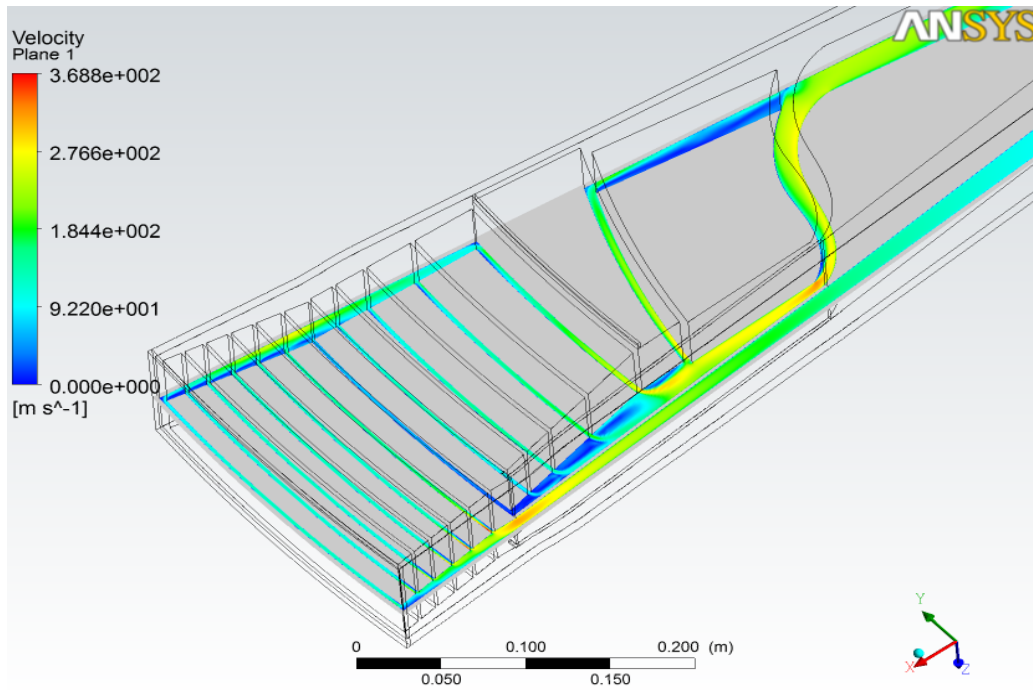


Figure 3 Low velocity behind slab 6

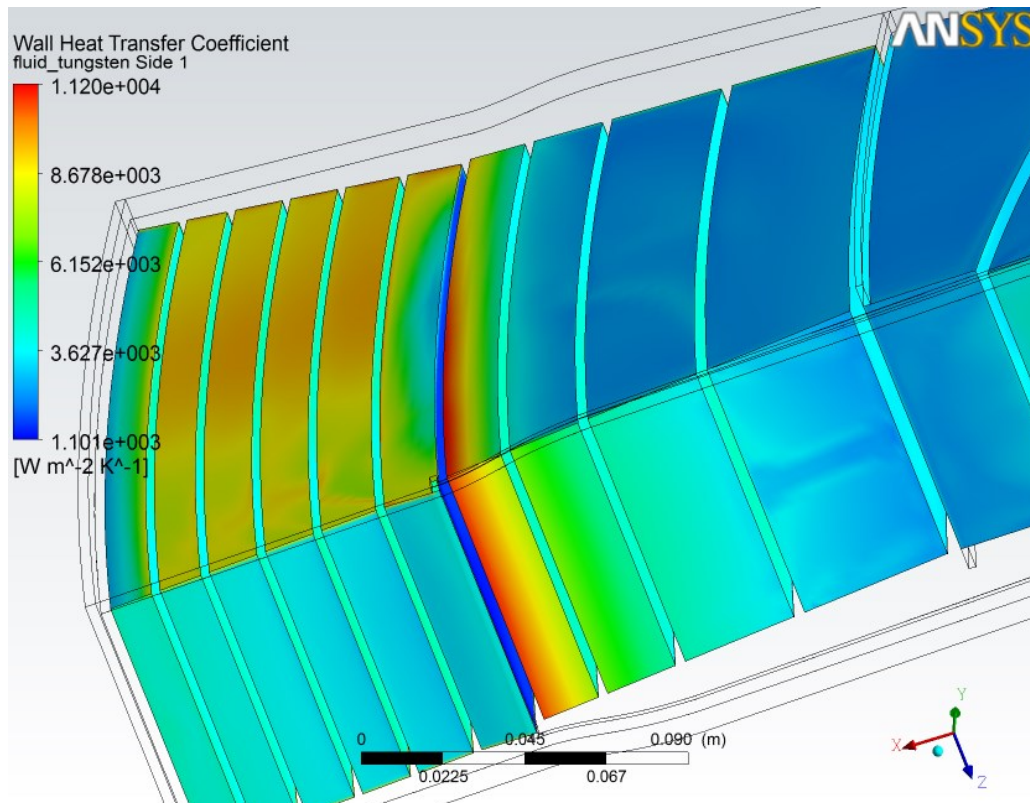


Figure 4 Low heat transfer coefficient on the back of slab 6

The tungsten slabs vary in temperature from 56°C to 500°C in the steady state model (Figure 5, Figure 6).

**B: Steady-State Thermal**  
 Temperature  
 Type: Temperature  
 Unit: °C  
 Time: 1  
 27/09/2012 15:07

**ANSYS**  
 14.0

**500.7 Max**  
 451.31  
 401.92  
 352.54  
 303.15  
 253.76  
 204.37  
 154.99  
 105.6  
**56.211 Min**

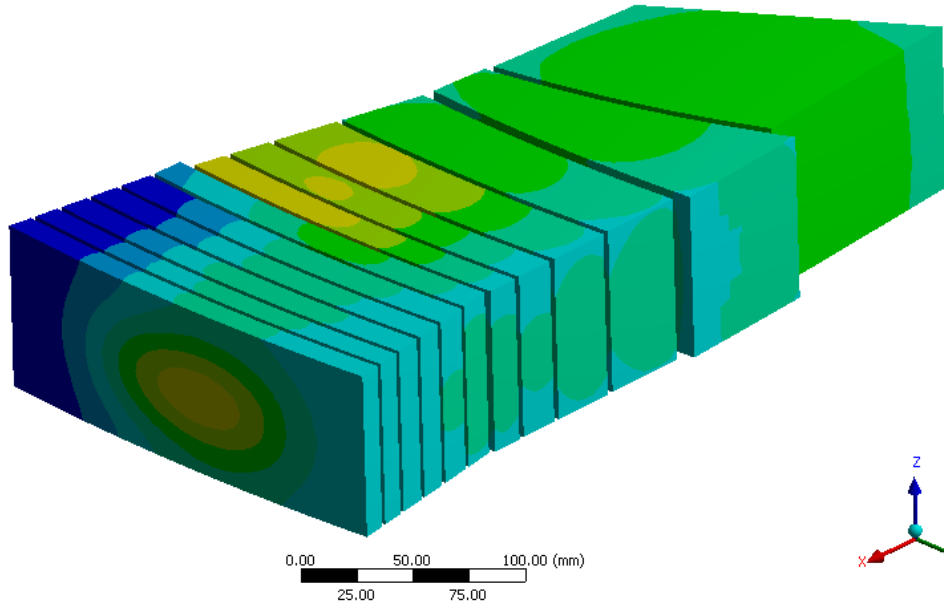


Figure 5 Steady state temperature profile a

**B: Steady-State Thermal**  
 Temperature  
 Type: Temperature  
 Unit: °C  
 Time: 1  
 27/09/2012 15:08

**ANSYS**  
 14.0

**500.7 Max**  
 451.31  
 401.92  
 352.54  
 303.15  
 253.76  
 204.37  
 154.99  
 105.6  
**56.211 Min**

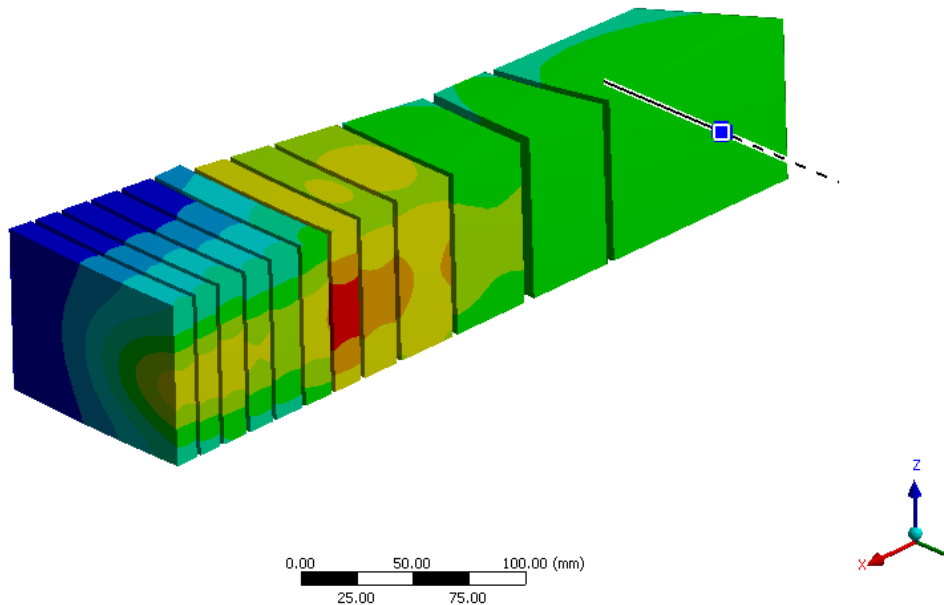


Figure 6 Steady state temperature profile b

The proposed helium cooled tungsten wheel rotates at 25rpm and the beam pulses at 14Hz. This result in each segment of the wheel seeing a beam pulse every 2.36seconds. As such the beam heating of the tungsten slabs is very much a cyclic process. The 2.5GeV proton beam pulse results in a peak temperature jump in the tungsten of 140K every 2.36seconds. A transient thermal analysis has been completed in order to predict the tungsten temperature profile immediately before and after the beam pulse. Several beam pulses are applied in order to reach a steady condition where the target is no longer heating up on a long

timescale and just sees a repetitive temperature variation from the repeating pulse. While the energy deposition is dynamic in the transient simulation the CFD model which calculates the helium flow is not solved on a transient basis due to the computationally intensive nature of such a calculation. As such the heat transfer coefficient and wall adjacent temperatures calculated in the steady state calculation are applied as a constant cooling function throughout the transient analysis. While some variation in helium temperature, velocity and heat transfer coefficient would occur during the transient it is thought reasonable to ignore these as secondary effects. After the target segment has received multiple pulses (Figure 11) and reached its maximum temperature the temperature contours before and after a pulse are calculated. The temperature range immediately before a pulse, i.e. after 2.36s of cooling is 54°C to 474°C (Figure 7, Figure 8) and the temperature range immediately after a pulse is 57°C to 546°C (Figure 9, Figure 10).

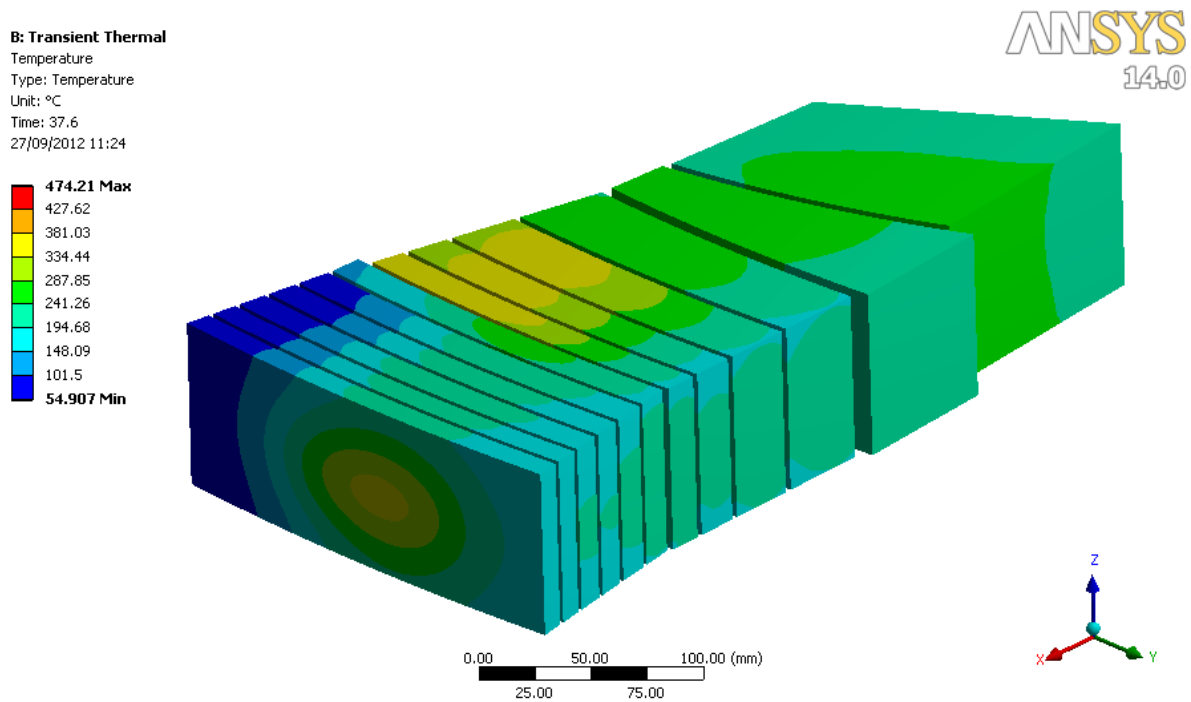
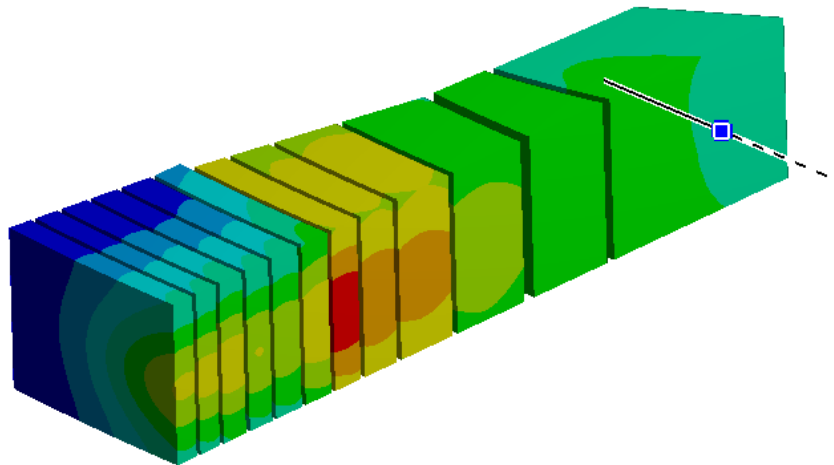


Figure 7 Temperature profile immediately before pulse a

**B: Transient Thermal**  
Temperature  
Type: Temperature  
Unit: °C  
Time: 37.6  
27/09/2012 11:24

**ANSYS**  
14.0

474.21 Max  
427.62  
381.03  
334.44  
287.85  
241.26  
194.68  
148.09  
101.5  
54.907 Min



0.00 50.00 100.00 (mm)  
25.00 75.00

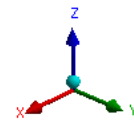
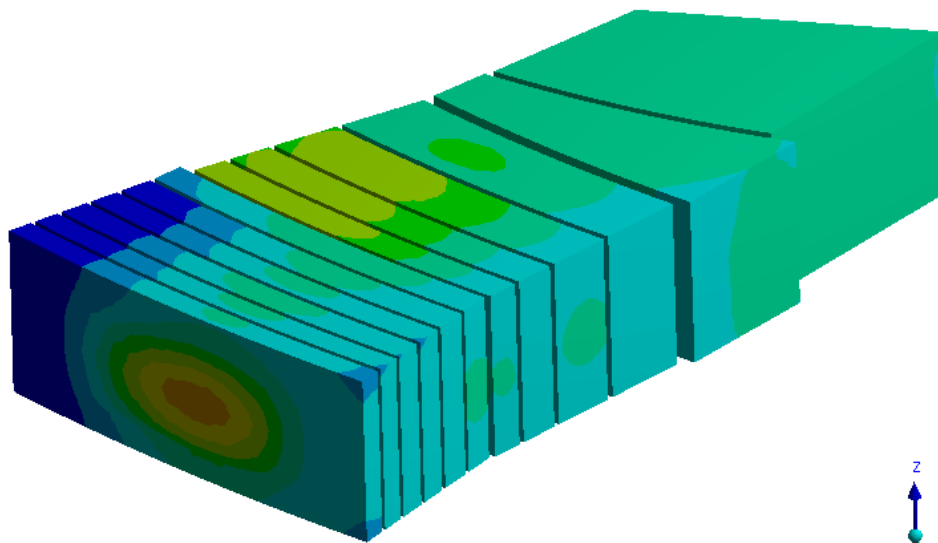


Figure 8 Temperature profile immediately before pulse b

**B: Transient Thermal**  
Temperature  
Type: Temperature  
Unit: °C  
Time: 37.603  
27/09/2012 11:23

**ANSYS**  
14.0

546.39 Max  
492  
437.61  
383.22  
328.82  
274.43  
220.04  
165.65  
111.26  
56.869 Min



0.00 50.00 100.00 (mm)  
25.00 75.00

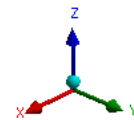


Figure 9 Temperature profile immediately after pulse a

**B: Transient Thermal**  
 Temperature  
 Type: Temperature  
 Unit: °C  
 Time: 37.603  
 27/09/2012 11:23

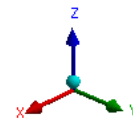
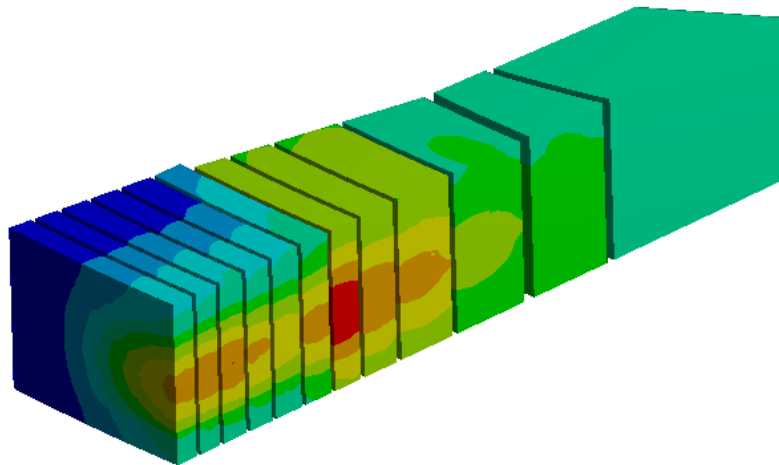
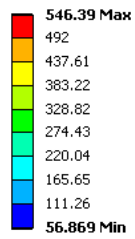


Figure 10 Temperature profile immediately after pulse b

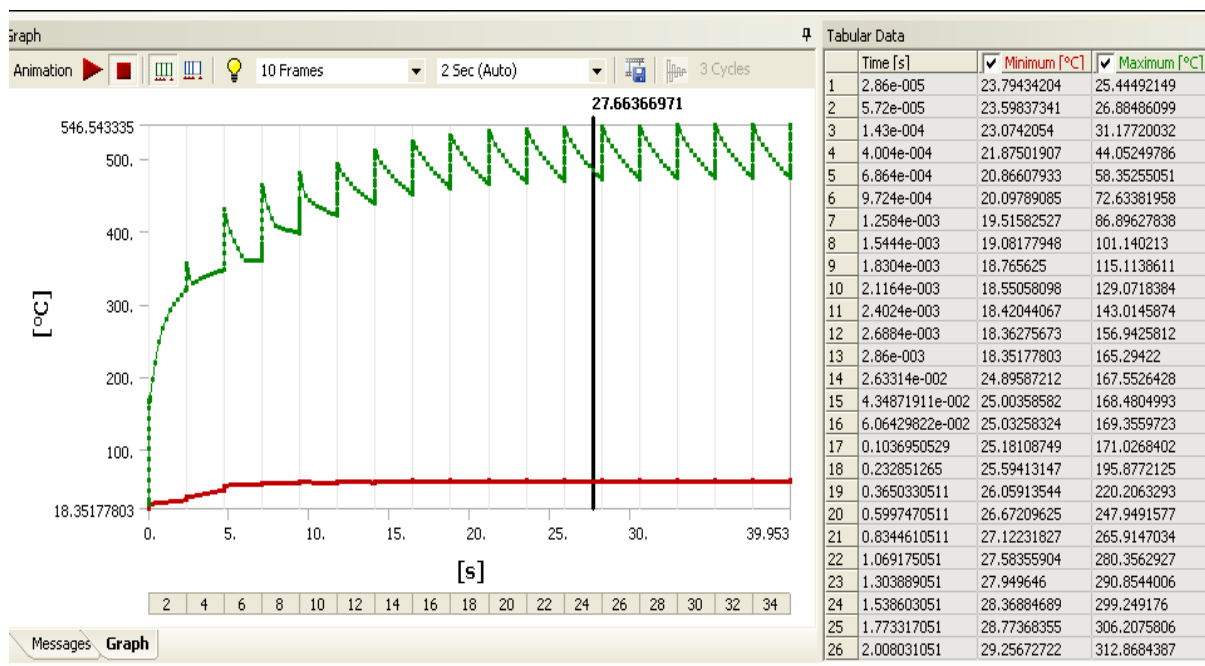


Figure 11 Maximum and minimum tungsten temperature during thermal transient model

## 1.2 Stress Model

As a result of the temperature contours within the tungsten slabs stress is induced. Typically targets can be subjected to quasi static stresses and inertial stresses. Quasi static stresses are those that result from relatively long lived thermal gradients. As for example with this design the tungsten slabs continuously have a temperature gradient during operation, it varies due to thermal conduction during the cool down between pulses but some thermal gradient and thus quasi static stress will exist as long as the slabs are being non uniformly heated and cooled. Inertial stresses occur if the heating from the beam occurs so rapidly that the target material is heated before it has time to expand. This results in an inertial effect where the material starts expanding and then overshoots and is manifested in the form of stress waves oscillating throughout the target. A simple test to identify if inertial stress is a problem is to compare the energy deposition time with the expansion time of the target. In this case the beam pulse is 2.86ms and the expansion time of the slabs is just a characteristic dimension divided by the sound speed. The expansion time can be estimated as the width of the slabs divided by the shear sound speed in tungsten i.e.  $0.2\text{m}/2884\text{m/s} = 70\text{microseconds}$ . As this is much smaller than the beam pulse inertial stresses are neglected in this stress evaluation.

The quasi static stress calculated from the steady state temperature contour (i.e. time averaged power input) yield a peak Von-Mises stress of 225MPa (Figure 12, Figure 13). Temperature dependant properties for the tungsten are assumed as per Appendix 4.2. The peak quasi static stress calculated from the temperature contours prior to a beam pulse is 217MPa (Figure 14, Figure 15), but immediately after the beam pulse the increased thermal gradients result in a peak stress of 340MPa (Figure 16, Figure 17). The peak deflection of the tungsten is 0.18mm and occurs at plate 7 (Figure 18).

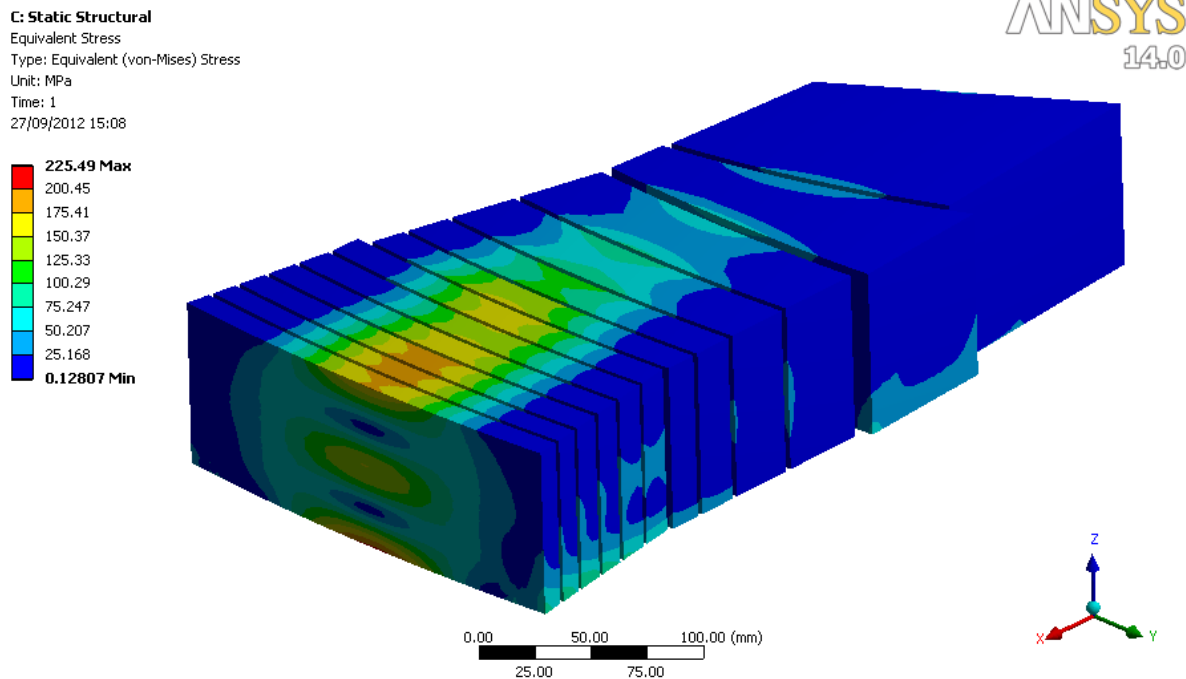


Figure 12 Steady state Von-Mises equivalent stress in tungsten target plates.

C: Static Structural  
Equivalent Stress  
Type: Equivalent (von-Mises) Stress  
Unit: MPa  
Time: 1  
27/09/2012 15:08

ANSYS  
14.0

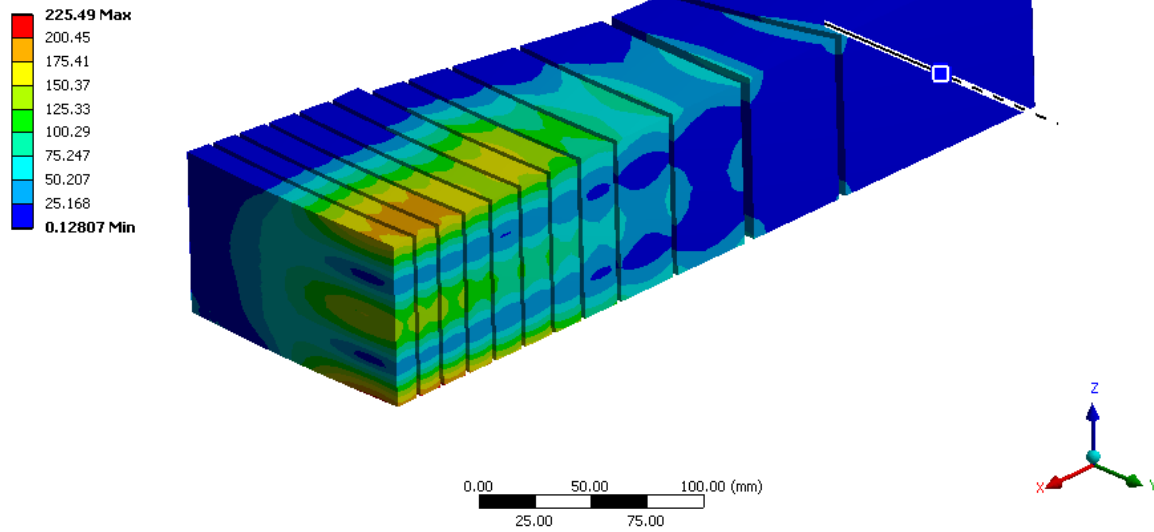


Figure 13 Cross-sectional view of steady state Von-Mises equivalent stresses in tungsten target plates

C: Static Structural  
Equivalent Stress  
Type: Equivalent (von-Mises) Stress  
Unit: MPa  
Time: 1  
27/09/2012 11:20

ANSYS  
14.0

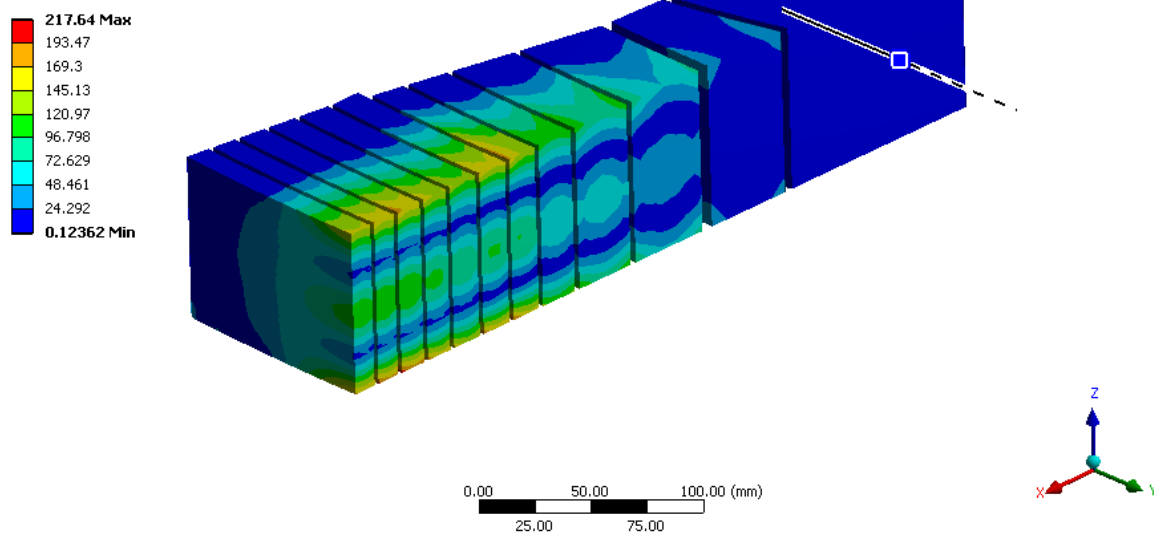


Figure 14 Cross-sectional view of Von-Mises equivalent stresses in tungsten target plates immediately before beam pulse.

C: Static Structural  
Equivalent Stress  
Type: Equivalent (von-Mises) Stress  
Unit: MPa  
Time: 1  
27/09/2012 11:13

ANSYS  
14.0

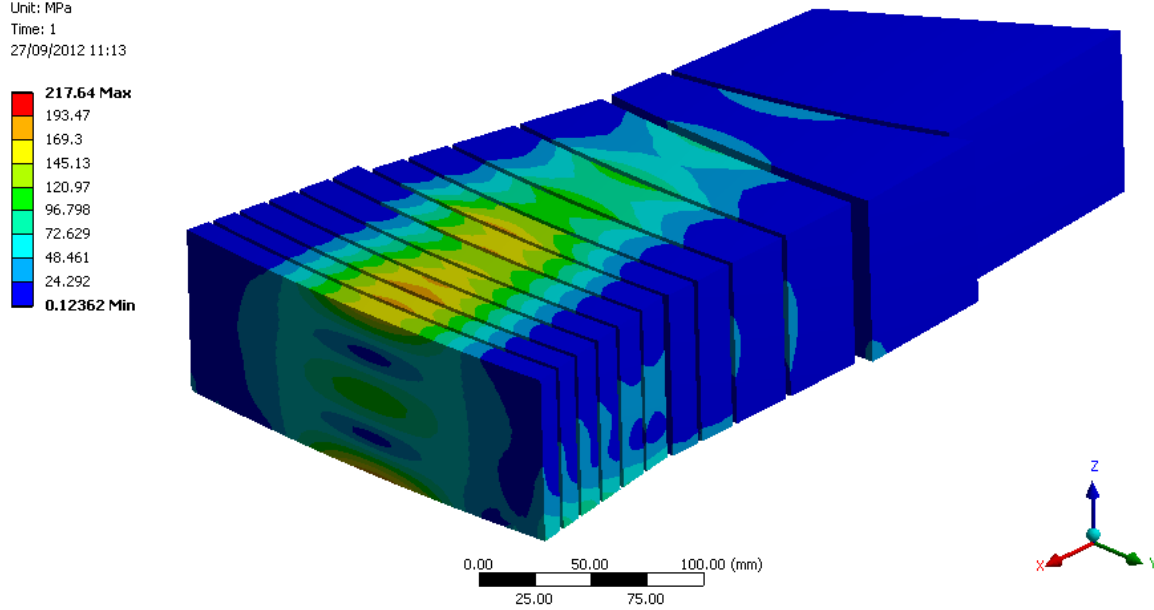


Figure 15 Von-Mises equivalent stresses in tungsten target plates immediately before beam pulse.

C: Static Structural  
Equivalent Stress  
Type: Equivalent (von-Mises) Stress  
Unit: MPa  
Time: 1  
27/09/2012 11:01

ANSYS  
14.0

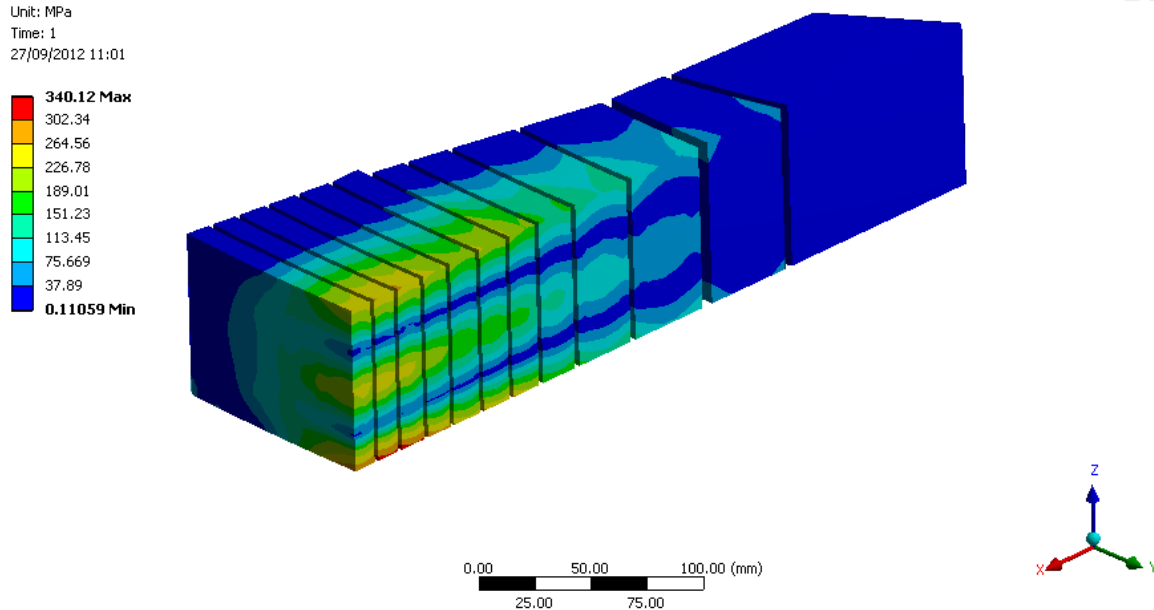


Figure 16 Cross-sectional view of Von-Mises equivalent stresses in tungsten target plates immediately after beam pulse

C: Static Structural  
 Equivalent Stress  
 Type: Equivalent (von-Mises) Stress  
 Unit: MPa  
 Time: 1  
 27/09/2012 11:02

ANSYS  
 14.0

340.12 Max  
 302.34  
 264.56  
 226.78  
 189.01  
 151.23  
 113.45  
 75.669  
 37.89  
 0.11059 Min

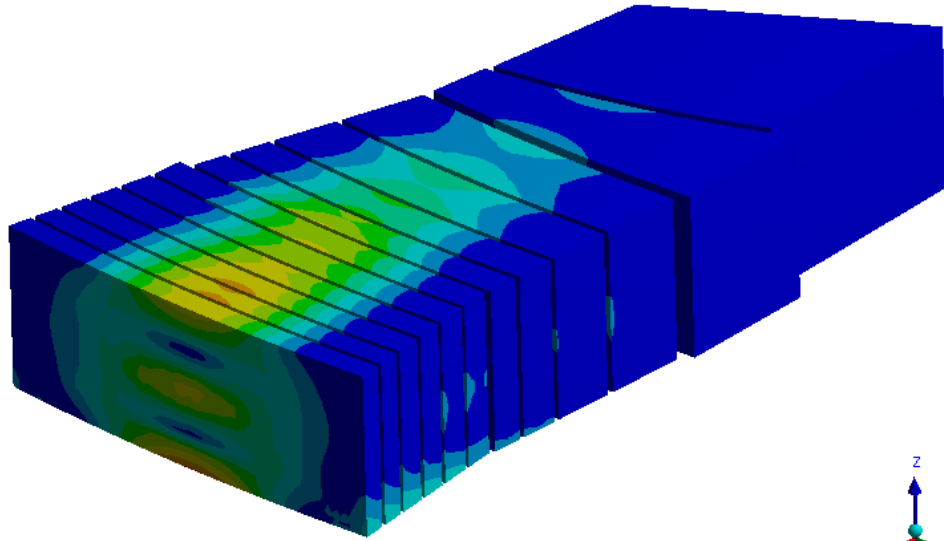


Figure 17 Von-Mises equivalent stresses in tungsten target plates immediately after beam pulse.

C: Static Structural  
 Total Deformation  
 Type: Total Deformation  
 Unit: mm  
 Time: 1  
 23/01/2013 13:37

ANSYS  
 14.0

0.18626 Max  
 0.16561  
 0.14495  
 0.1243  
 0.10364  
 0.082988  
 0.062333  
 0.041678  
 0.021023  
 0.00036769 Min

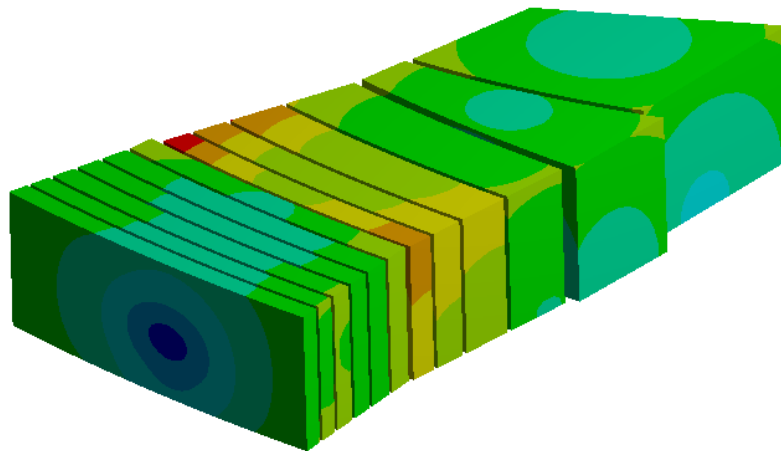


Figure 18. Peak displacement in tungsten target plates immediately after beam pulse.

### 1.3 Discussion

The predicted peak stress levels in the tungsten slabs of 340MPa with a fluctuation of 120MPa are concerning. Figure 19 shows the yield strength of tungsten in various forms. At 500°C the yield strength of stress relieved thin sheet are well in excess of the calculated levels however 25mm diameter rod is only just over 400MPa at 500°C. Typically the endurance limit of material is significantly less than the yield strength and as the loading is of a cyclic nature fatigue cracking of the tungsten has to be a risk. Close investigation and testing of the physical properties of tungsten following the manufacturing process are highly recommended. In addition it is thought that reducing the size of the tungsten slabs so as to increase heat transfer area and reduce temperature gradients would result in a more conservative design. At the

limit one may consider a packed sphere target in order to get maximum surface to volume ratio. Some alternative ideas are presented in the following sections.

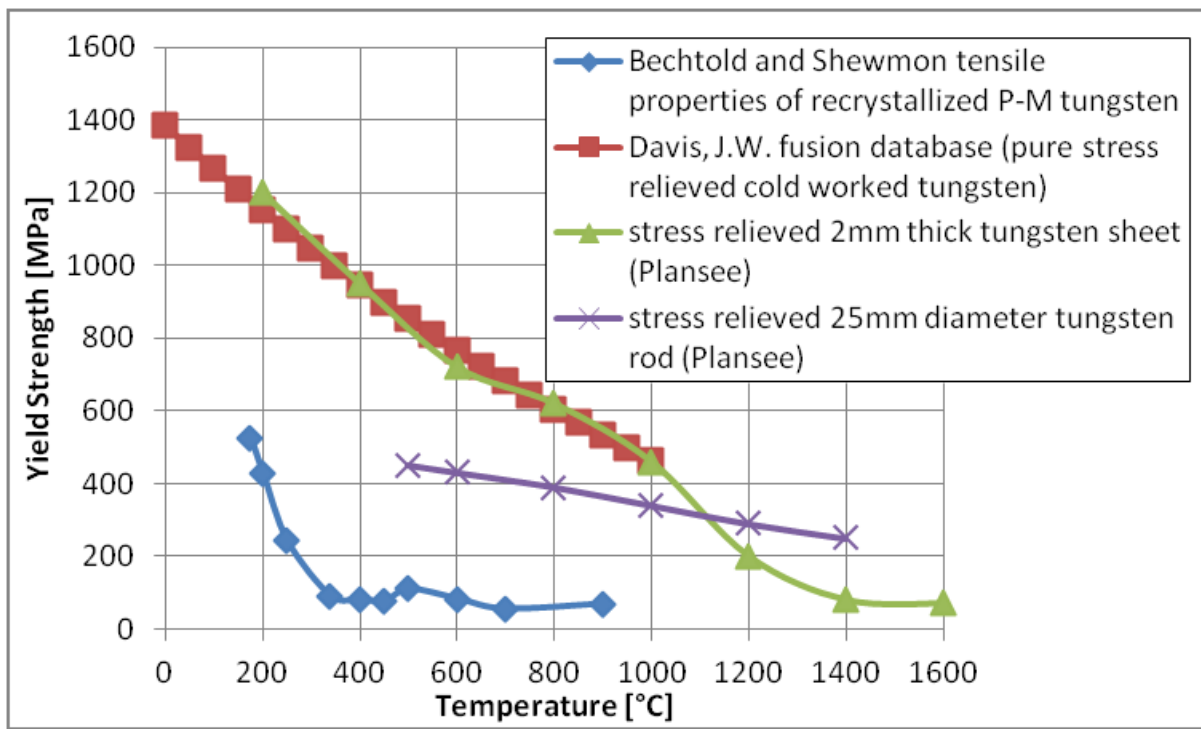


Figure 19 Yield Stress of Tungsten of various specifications

## 2 A “sunflower” packed bed target design for ESS

The current plates based target baseline offers a relatively effective solution which falls within acceptable thermal parameters. In previous work, the design of the plates was optimised to maintain the temperature of the tungsten below the design value of around 500C whilst keeping the velocity of the cooling helium well below the Mach number and the pressure drop to about 0.6bar. However, whilst effective from a thermal point of view, the previous section highlights that the thermal mechanical stresses in the target are high, particularly considering the cyclic nature of the load [3, 4] (Appendix 4.3) as well as the brittleness and anisotropy of tungsten [5]. So it seems reasonable to investigate an alternative arrangement of the target material which minimises the thermal mechanical stresses.

Considering that the duration of the beam pulse is relatively long compared with the time it takes for a sound wave to propagate in the target geometry (see Section 1), then dynamic inertial stresses are not likely to be of concern.

The design for the target should aim at minimising the cyclic thermal stress arising from every beam pulse. This is the heat signature left by the beam upon interaction with the target material which with the current baseline design parameters results in a peak temperature jump of around 150K.

After few minutes of operation with the beam pulsing at 14 Hz and full capacity helium cooling in place, the target will reach a peak operating temperature of around 500C (specified by the current baseline parameters). The location of this peak temperature is not at the point of maximum power deposition as it results from a combination of the cooling pattern with the beam heat load.

Robust mechanical design is required to withstand the thermal distortion from both the cyclic beam pulse and the maximum steady state temperature.

If starting to design from a solid ring of material (ideal for neutron production), then the target needs to be divided into smaller parts in order to minimise the stresses arising from the thermal distortion (as explained above) as well as providing enough cooling channels to maintain the temperature of the material below the required 500C.

Target segmentation is effective in reducing both the thermo-mechanical stresses and the operating temperature of the target. On the other hand segmentation of the target reduces the solid fraction to the detriment of the neutron production efficiency. Also a larger number of parts increases complexity which impacts adversely on reliability (the reliability of an assembly is often defined as the product of the reliability of each component).

Previous work at RAL investigated the effects of segmentation of the target into a granular structure. This Section presents the operating parameters of one granular target solution (not fully optimised) which is believed capable of bringing the thermal mechanical stress well below 100MPa. An outline design of the mechanical and functional integration of such a concept is presented here.

## 2.1 Design of a granular target and supporting structure

The sample model presented here is obtained segmenting the target ring into 80mm tall grains with a series of helium channels geometrically defined by a mirrored circular pattern. The helium channels are 2mm wide and have constant cross section. Figure 20 shows the construction of the pattern used to obtain the helium channels.

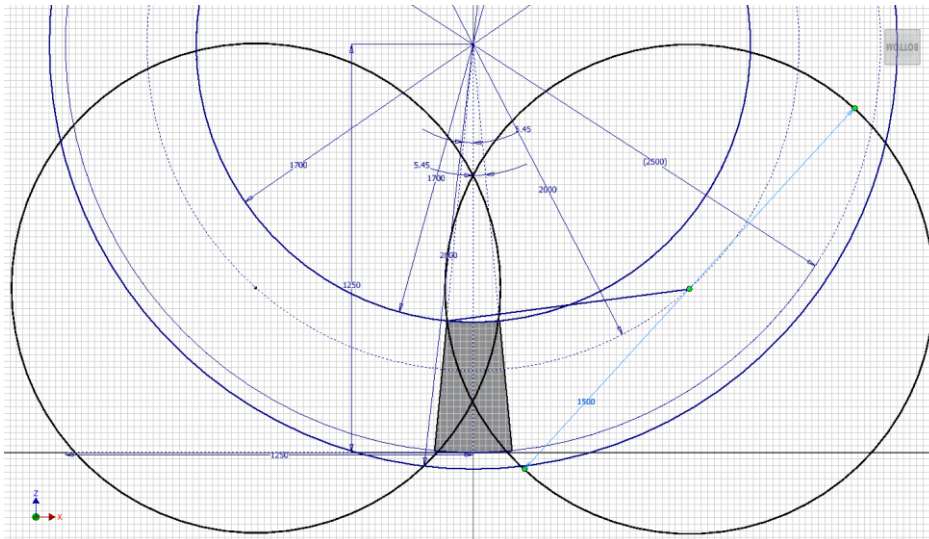


Figure 20. Construction pattern of the helium channels

Figure 21 shows a typical grain segmentation obtained with the pattern in Figure 20. Figure 21 shows 80mm tall grains in a sector of 1/33 of the complete ring. This segmentation pattern and helium channel width offer a solid to gas fraction of approximately 86%. Note that in this design the sector presented (1/33 of the full ring) is not functionally defined but simply used for ease of modeling and representation. In practice the complete target ring would be made up of a continuum of grains. The 1/33 sector definition works well for the modeling as it contains entirely the energy deposition from one beam spill.

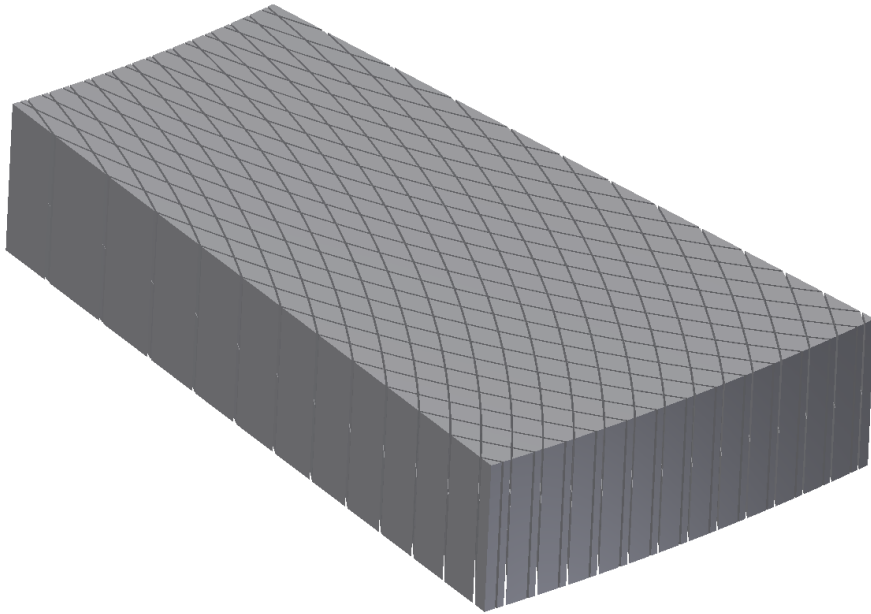


Figure 21. Sector of tungsten grains

Figure 22 shows a section of the whole target wheel with grains in pink. Note that the grains are mounted onto a solid hub (orange in the Figure) which provides support as well as a network of distribution channels for the helium coolant.

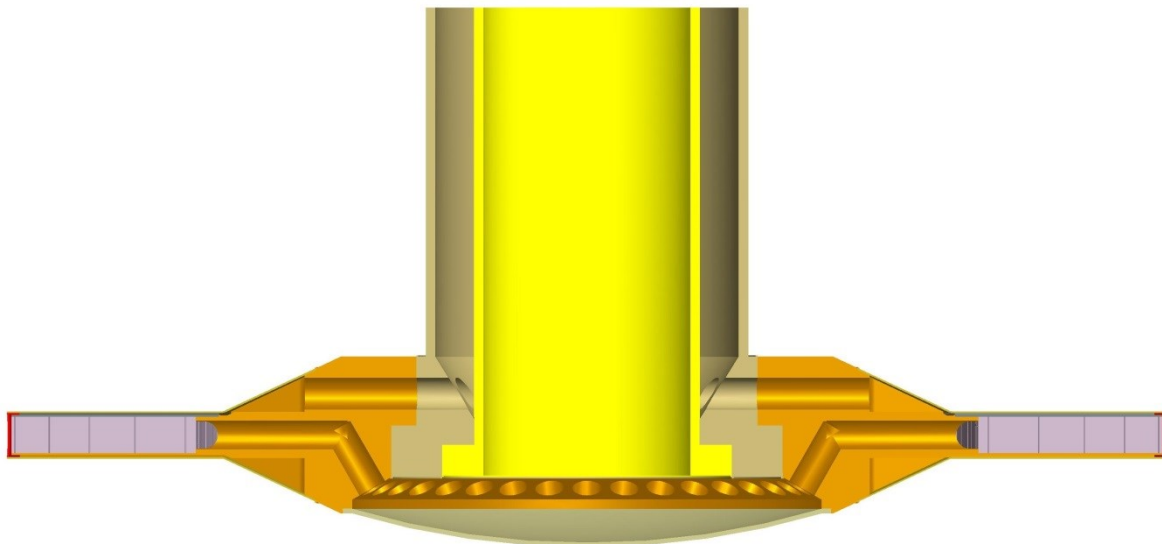


Figure 22. Section view of the entire target wheel supporting the granular structure (purple)

Figure 23 shows a section view of the target wheel with a functional diagram for the helium flow. The target grains are supported between two annular 'sandwich' plates to form a solid structure. This assembly

is integrated with the outer helium vessel so as to transfer the mechanical loads resulting from the helium pressure through the target material.

Here the grains are located on grooves on the annular plates (defining the helium channels) and brazed in position as well as retained by small axial tungsten screws or rivets as is common practice on high temperature assemblies. The blue line represents the cold helium entering through the outer annulus of the wheel shaft. The helium then enters the orange solid hub which distributes it via a series of alternating channels to the top and bottom of the target ring. Here the helium flows radially outwards in flat channels above and below the target sandwich structure, thus providing direct cooling of the surrounding vessel walls, shown in purple in the Figure. The top and bottom flows join and reverse at the beam window (periphery of the wheel) and then flow through the matrix of the grains providing the required cooling. Note that the return channels for the helium in the solid hub are alternated with the distribution channels for the supply gas. Finally the hot helium (red line) returns to the cooling plant via the core of the shaft.

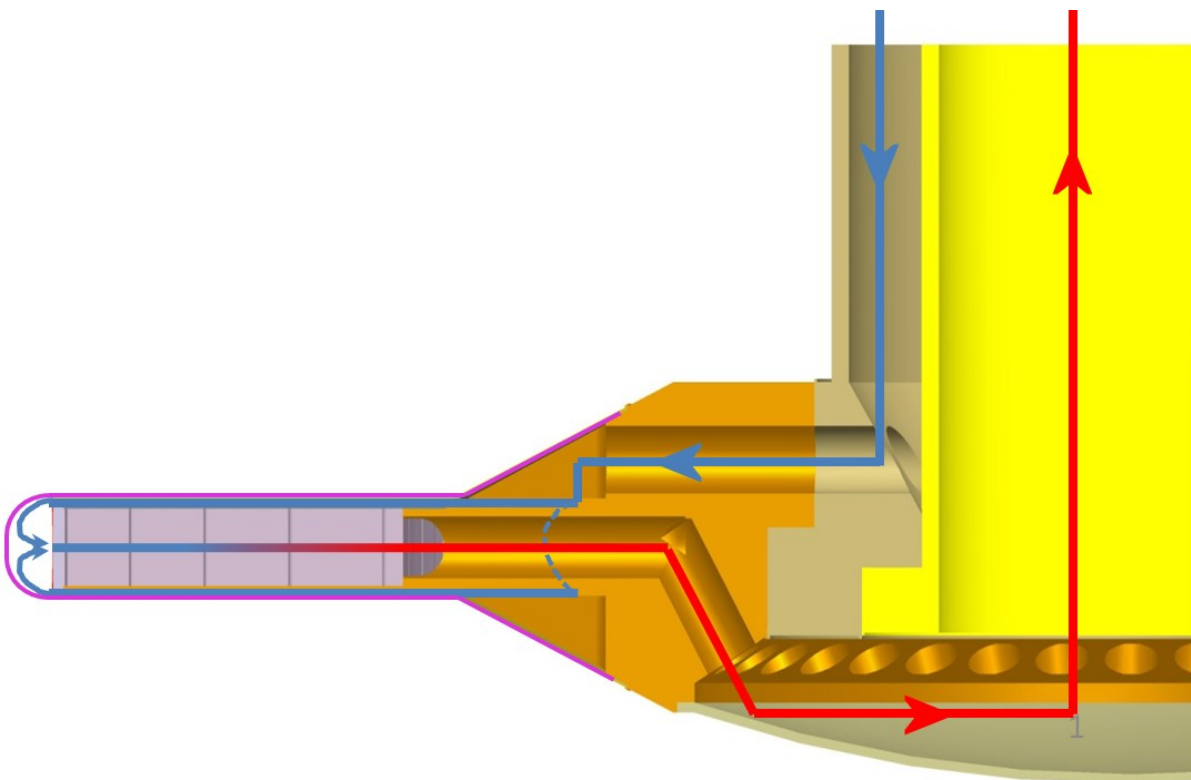
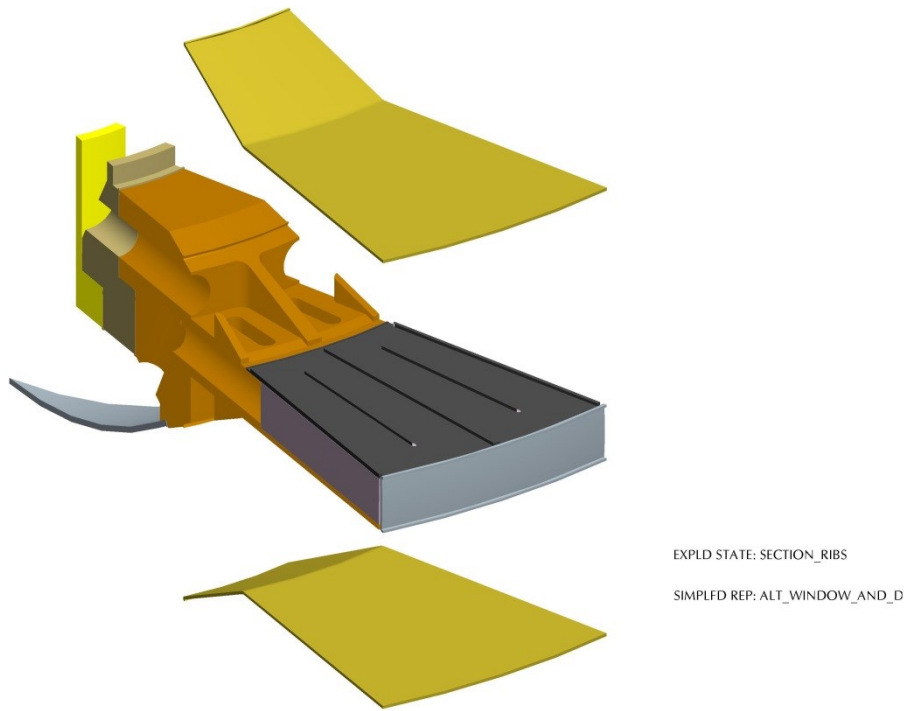


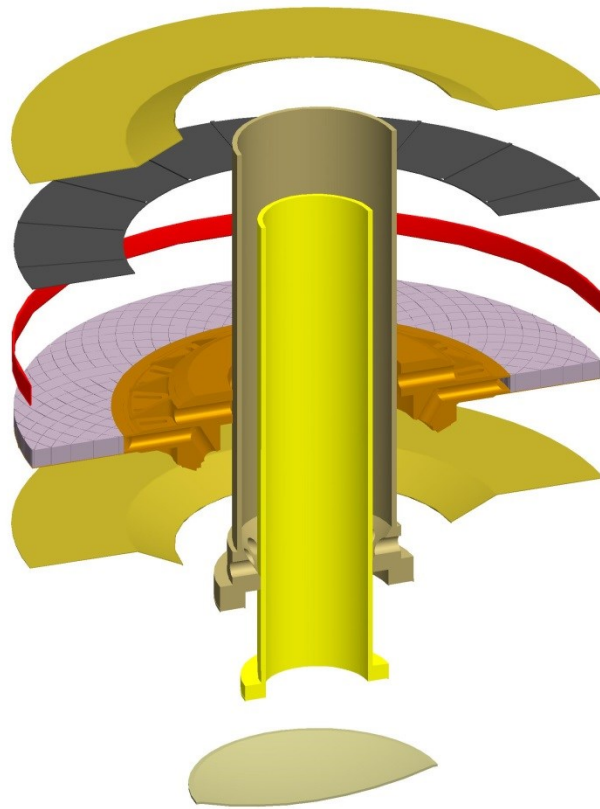
Figure 23. Section of the target wheel with functional helium flow path

Figure 24 shows an exploded sector of target with a pair of supply and return channels through the solid hub (orange). Note that plates which sandwich the target grains (dark grey in the Figure) are ribbed to provide the support for the outer vessel skins (dark yellow in Figure).



**Figure 24. Functional break down of the target wheel**

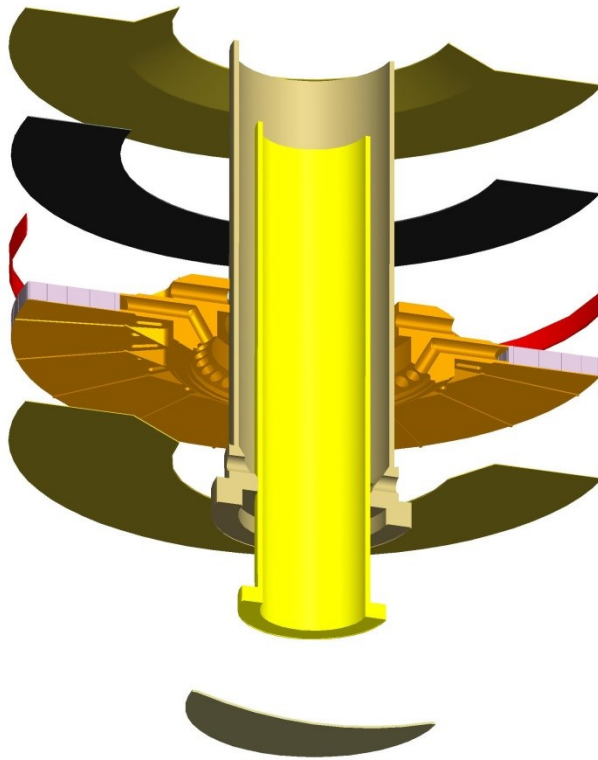
Figure 25 shows an exploded section of the target wheel. Here the grains are in pink, the beam window is red, the solid hub orange, the top sandwich plate in dark grey and the outer skin is dark yellow.



EXPLD STATE: ASSEMBLE

Figure 25. Exploded top view of the components making up the target wheel

Figure 26 shows a similar exploded view from the bottom of the wheel. You can see here that the bottom plate which holds the grains (ribbed) is an integral part of the orange solid hub.



EXPLD STATE: ASSEMBLE

Figure 26. Exploded bottom view of the components making up the target wheel

The outer skins containing the helium flow are designed to be welded along the radial support ribs and the rim of the solid hub (Figure 24). This is necessary to prevent them from ballooning when pressurized with helium to the operating pressure of around 4bar. Figure 27 shows that this method is effective in achieving acceptable stresses of 36MPa in the outer shroud when the hub is pressurized. The stresses generated in the tungsten by transmitting these loads are significantly lower than the thermal stresses.

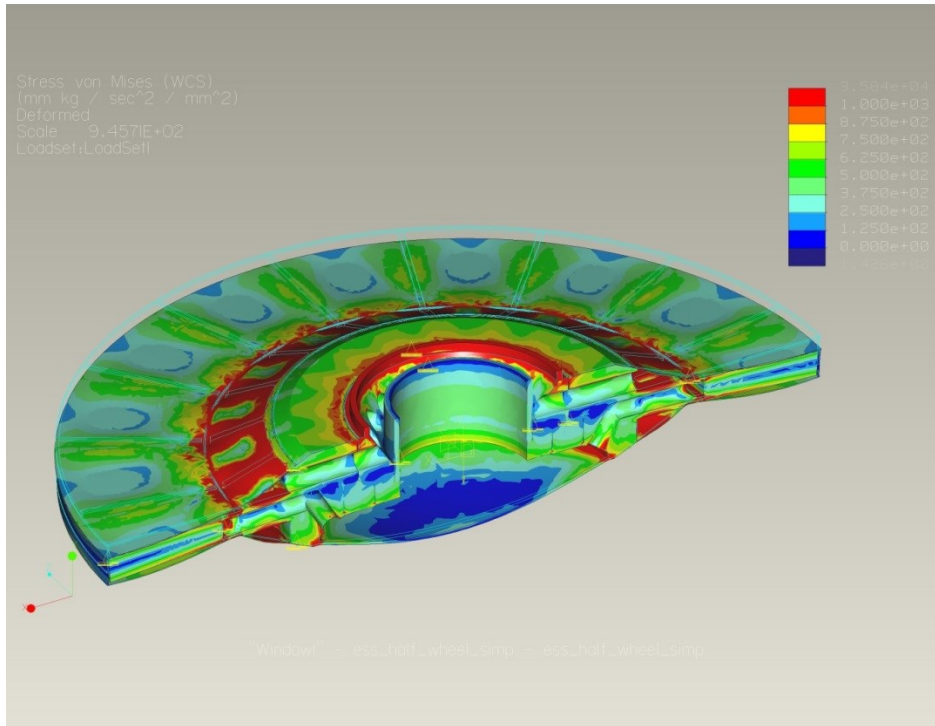


Figure 27. Equivalent Von Mises stresses arising from gravity and the helium pressurization of the target wheel vessel (units in kPa)

Figure 28 shows the maximum displacement of the target structure under its own weight.

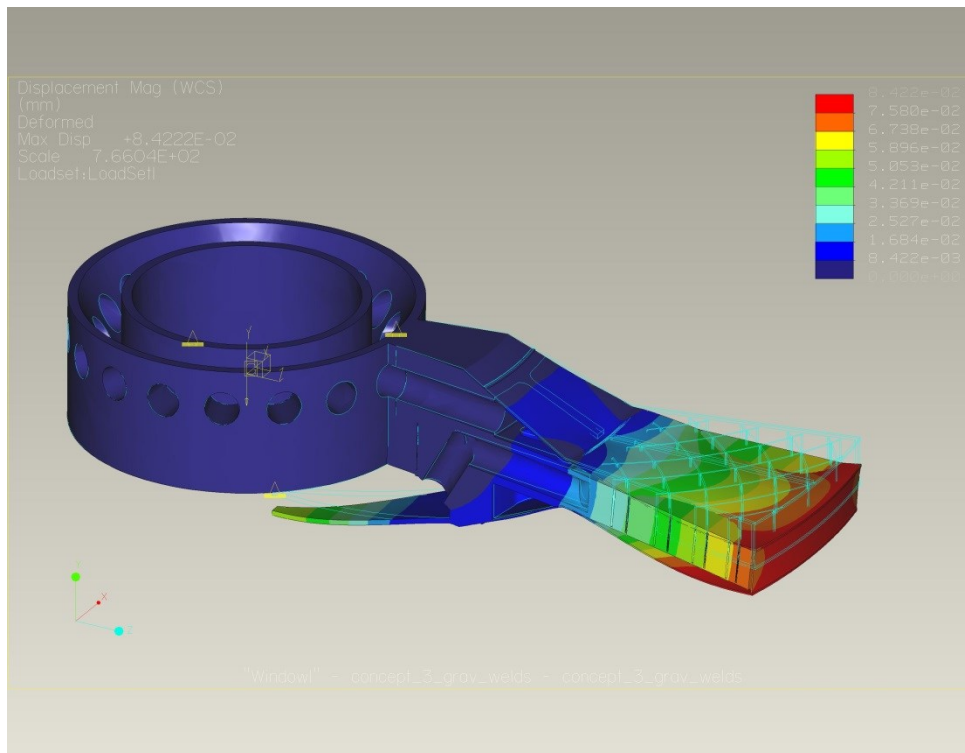


Figure 28. Maximum displacement of the target structure under its own weight [mm]

## 2.2 Thermal mechanical model of the beam heat signature

A model was developed to study the thermal mechanical response of the granular structure typified in Figure 21.

Figure 29 shows the thermal print left by one complete beam spill in the middle plane section of the grains in the sector.

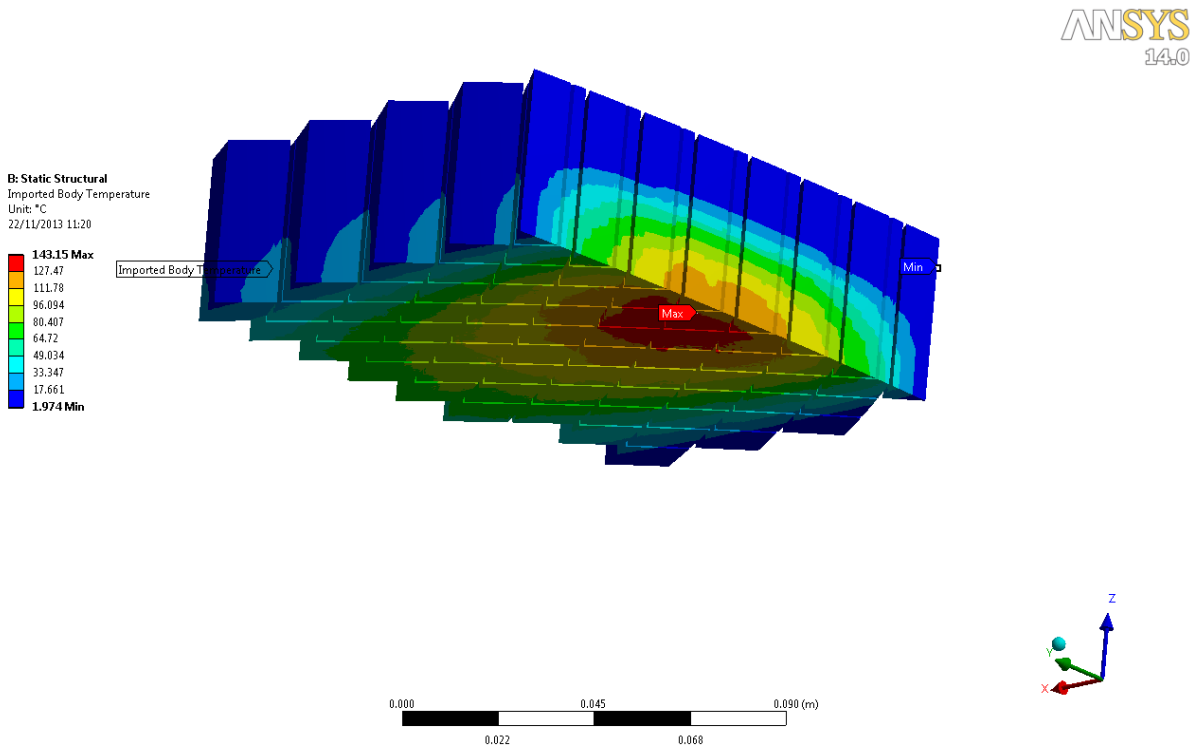


Figure 29. Temperature jump from one beam spill. Middle plane section

So at each beam pulse the temperature in the front grains cycles by around 150K. This generates a cyclic stress in the material which is simulated and reported as a Von Mises equivalent stress in Figure 30 and Figure 31. Note that the grains in this model have sharp edges and so it is likely that filleted grain corners would result (both in a simulation and in reality) in somewhat lower stress. Note that while the high temperature fatigue properties of tungsten may be unknown, the fatigue limit in the material is likely to be a fraction of its yield strength [4] (Appendix 4.3).

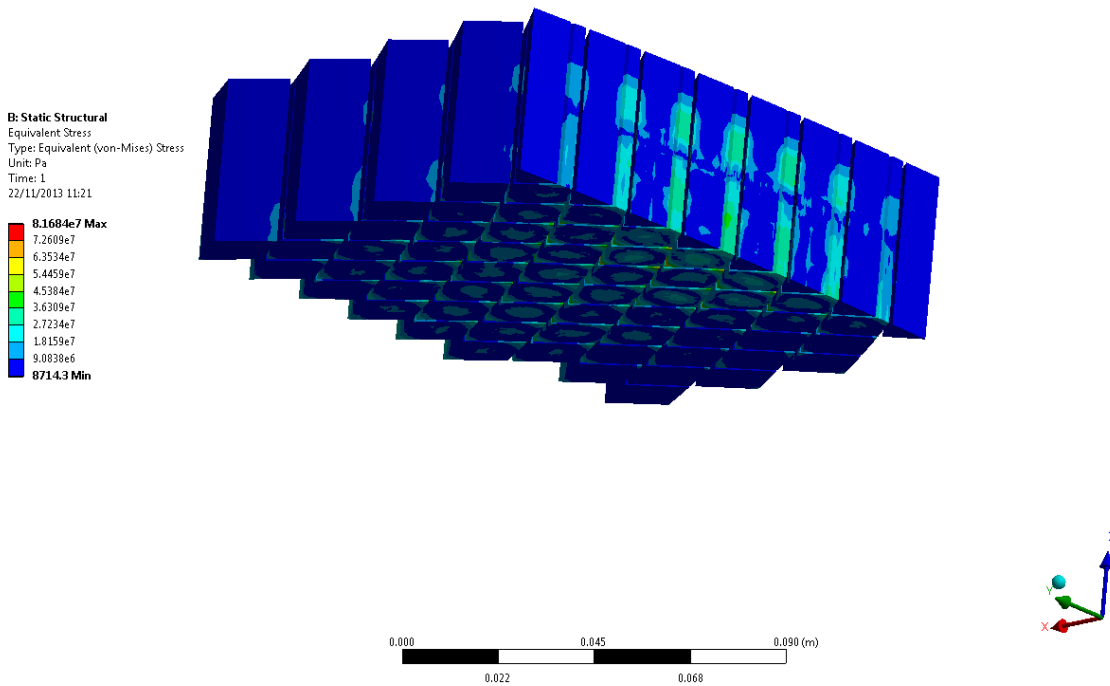


Figure 30. Von Mises stresses arising from one complete beam spill . Middle plane section

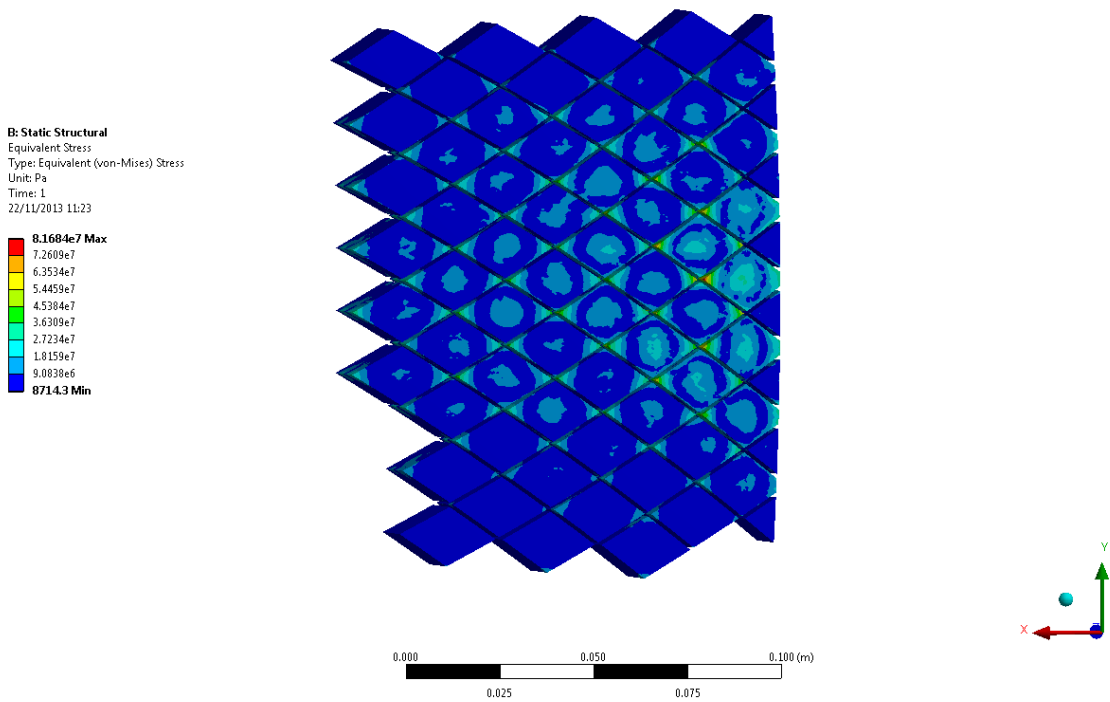


Figure 31. Von Mises stresses arising from one complete beam spill . Middle plane section

The total thermal deformation in the simulations appears small (of the order of 20  $\mu\text{m}$ ) as reported in Figure 32.

B: Static Structural  
Total Deformation  
Type: Total Deformation  
Unit: m  
Time: 1  
22/11/2013 11:24

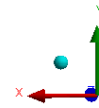
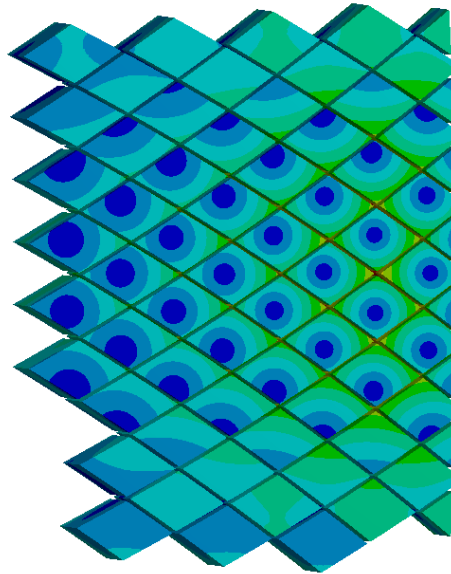
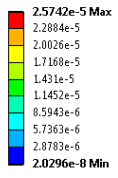


Figure 32. Total thermal deformation in the tungsten

### 2.3 Fluid mechanical steady state combined model

As mentioned earlier, the 1/33 sector of the ring here presented is not functional. In the case of a non-rastered beam the wheel would be spinning slowly so that two subsequent beam heat signatures are adjacent, creating a nearly uniform peak temperature around the circumference. This beam arrangement would fit approximately twice as many beam prints along the circumference as compared with the current baseline design. This makes better use of the target material and would either half the operating temperature or the capacity of the required cooling plant. The same could be said for radiation damage which would be better distributed within the target material. For a rastered beam, there would be similar benefits for both target designs but the raster pattern could be significantly simpler in this case compared to that required for the current baseline plate-type arrangement.

This overlapping, effectively continuous beam pattern is unfortunately very difficult to simulate as it requires modelling of the whole wheel (computationally prohibitive).

So a conservative thermal model is presented here where the beam impinges 33 times along the circumference of the wheel (same as in the current baseline).

Figure 33 shows the steady state temperature reached in the grains when modelling the helium flowing radially from the periphery towards the center of the wheel and the beam heat load applied on 33 equidistant spots along the circumference. The helium injection was set by mass flow rate as 3kg/s for the whole wheel as specified by the current TDR. The pressure of the helium was set at around 3.5bar.

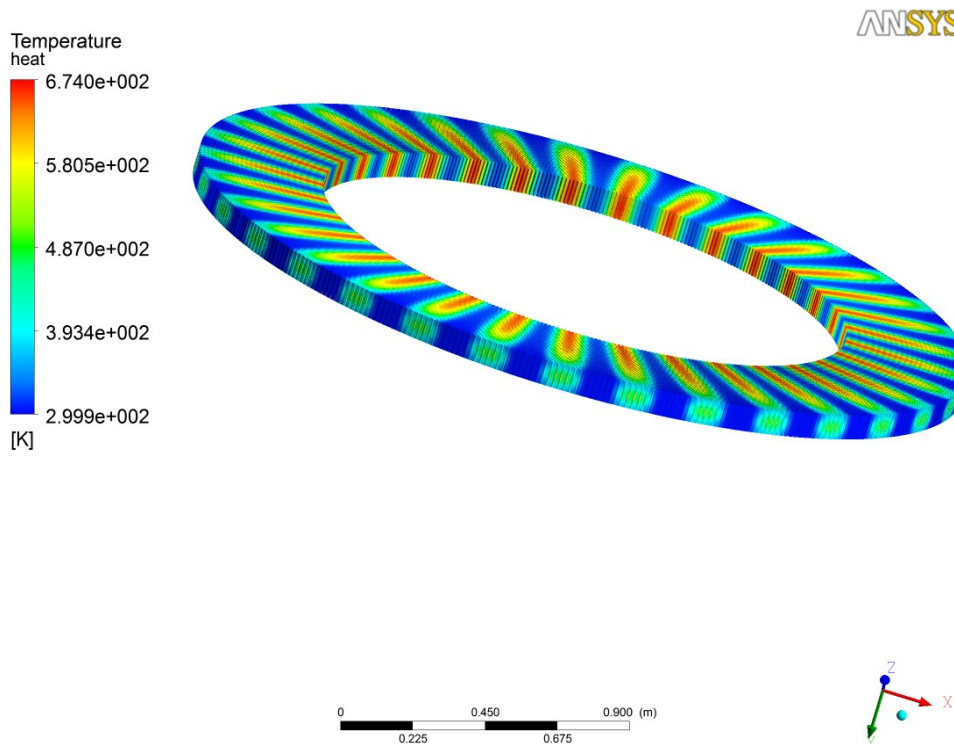


Figure 33. Steady state temperature of the complete target ring

Figure 34 and Figure 35 show respectively a vertical and horizontal section of the wheel which highlights the fact that although the beam print peaks near the periphery (Figure 29), the hottest region is in the grains near the midline of the ring. This is explained by the helium cooling path which flows through the grain matrix from the outer edge of the ring towards the middle of the wheel.

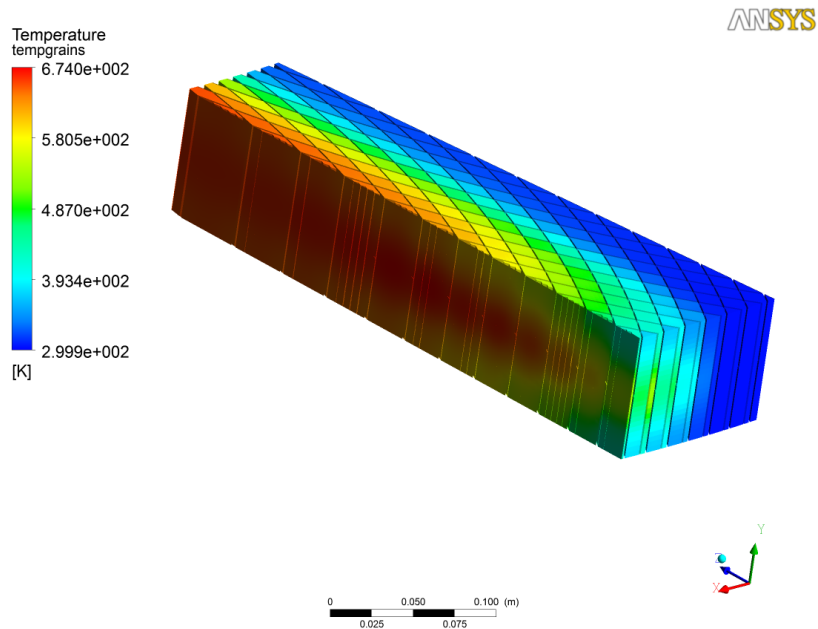


Figure 34. Peak steady state temperature in the target. Vertical section

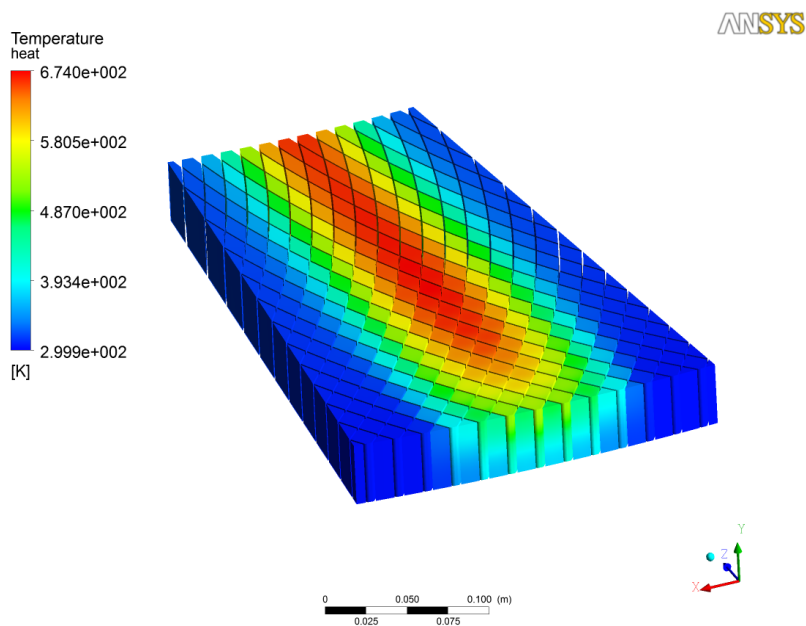


Figure 35. Peak steady state temperature in the target. Middle plane section of one target sector

Figure 36 shows the velocity of the helium in the cooling matrix. Note that the peak velocity is higher in the middle of the sector as the helium accelerates whilst acquiring heat from the grains.

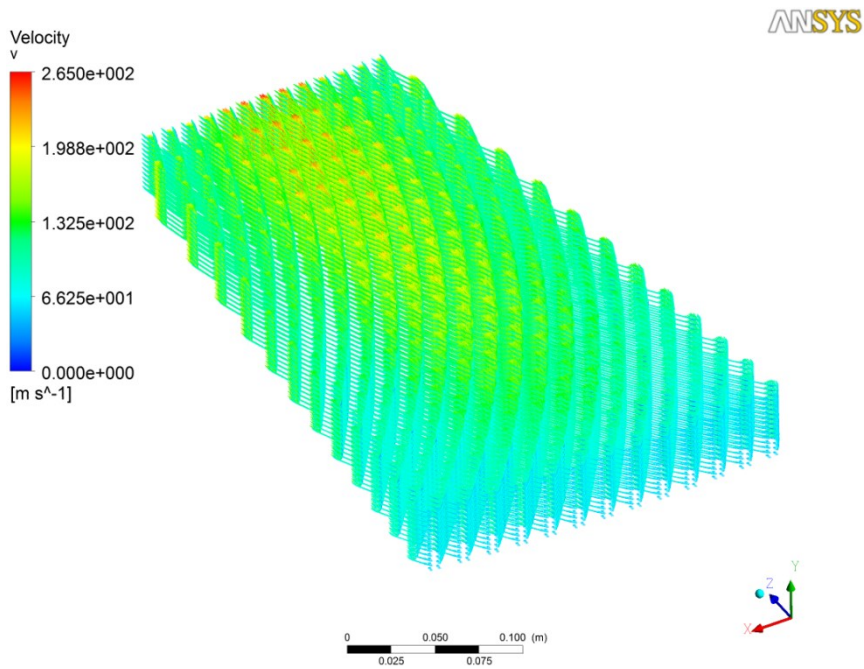


Figure 36. Peak helium velocity in the cooling channels

In spite of the uneven velocity field, Figure 37 shows that the pressure drop across the packed bed of grains is very uniform.

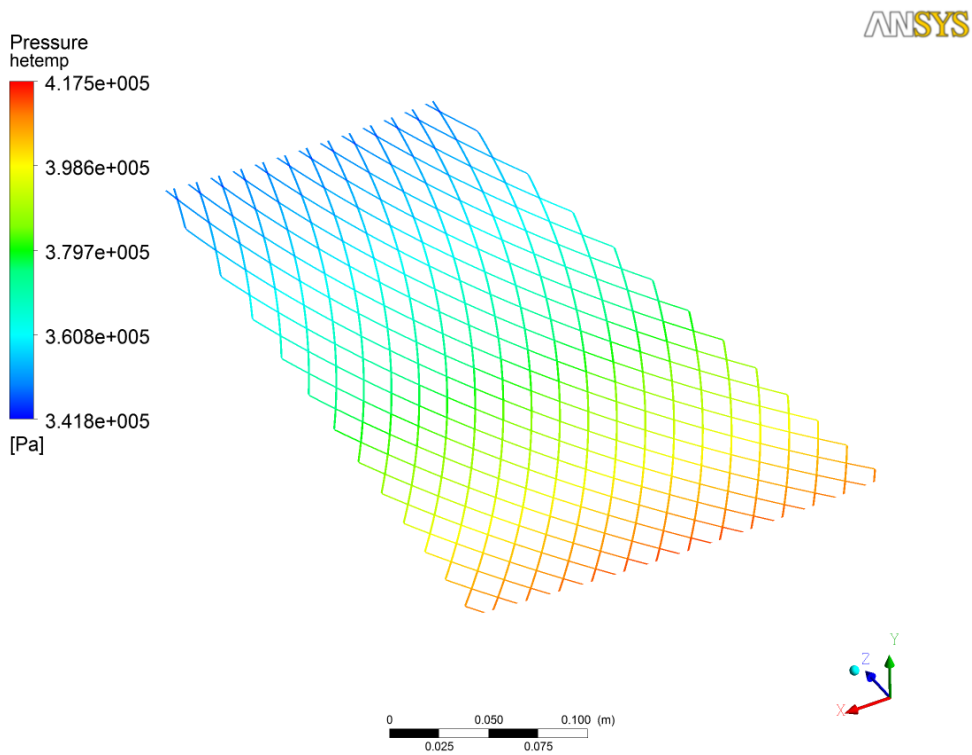
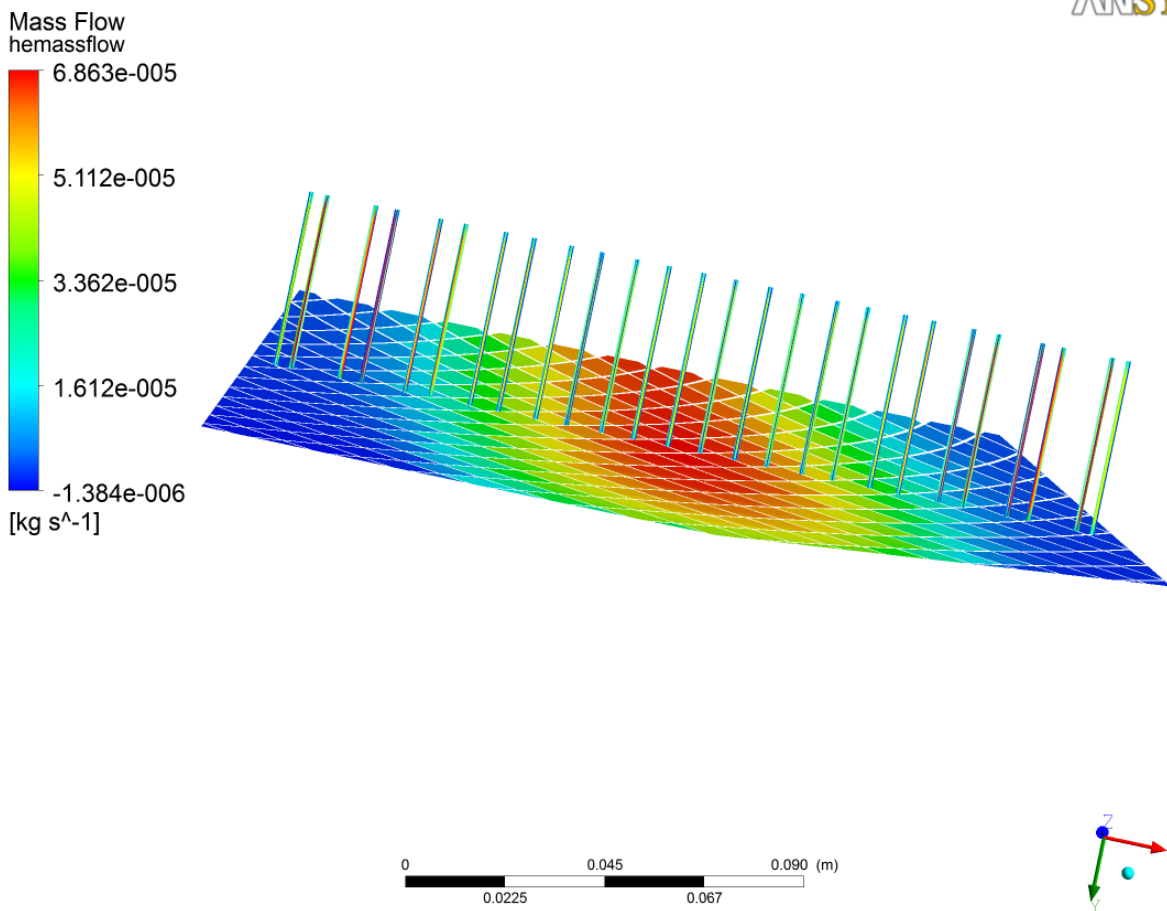


Figure 37. Helium pressure drop across the bed of grains

The vertical lines in Figure 38 show the helium mass flow rate through some of the cooling channels (the base plate represents a slice of the grains colored by temperature). Note that the mass flow rate of helium is higher (red) at the edges of the sector, where the material is cooler. This shows that although the helium has a preferential route towards the colder grains it is nevertheless driven by the uniform pressure drop to sufficiently cool all the grains (Figure 37) resulting in the steady state peak temperatures of Figure 35.



**Figure 38. Distribution of the mass flow of helium (vertical lines) with respect to one target sector (section plane colored by temperature)**

A sensitivity study of the grains based design to grain swelling is presented in Appendix 4.4. The sensitivity analysis suggests that channel shrinkage (due to grain swelling or assembly/machining tolerances) is unlikely to lead to overheating from run-away positive feedback.

## 2.4 Thermal mechanical “steady state”

After a few minutes of operation at 14Hz (i.e. several beam spills) the target will reach its peak operating temperature of around 470C (as specified by the current baseline) where the temperature will oscillate at each beam pulse as shown in Figure 39. So the beam footprint thermal stresses described in the previous section have to be supplemented by the steady-state component resulting from the higher operating temperature.

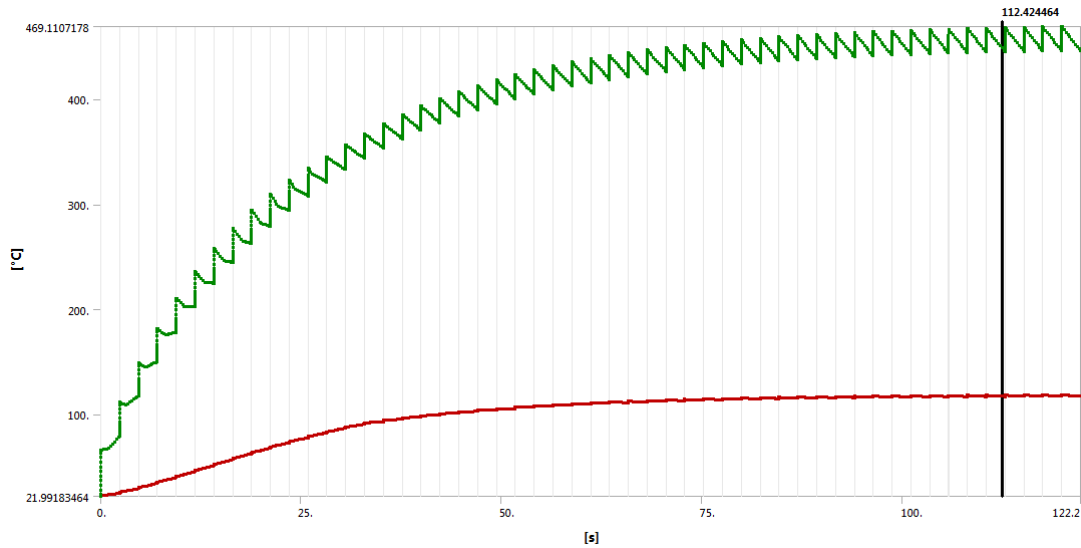


Figure 39. Transient thermal mechanical model. Startup temperature saw tooth

In order to study the thermal mechanical effect of the peak operating temperature a model was developed to study a few representative grains operating with the quasi-steady state temperature distribution. The grains studied in this model are the ones subtracted from the sector in Figure 40.

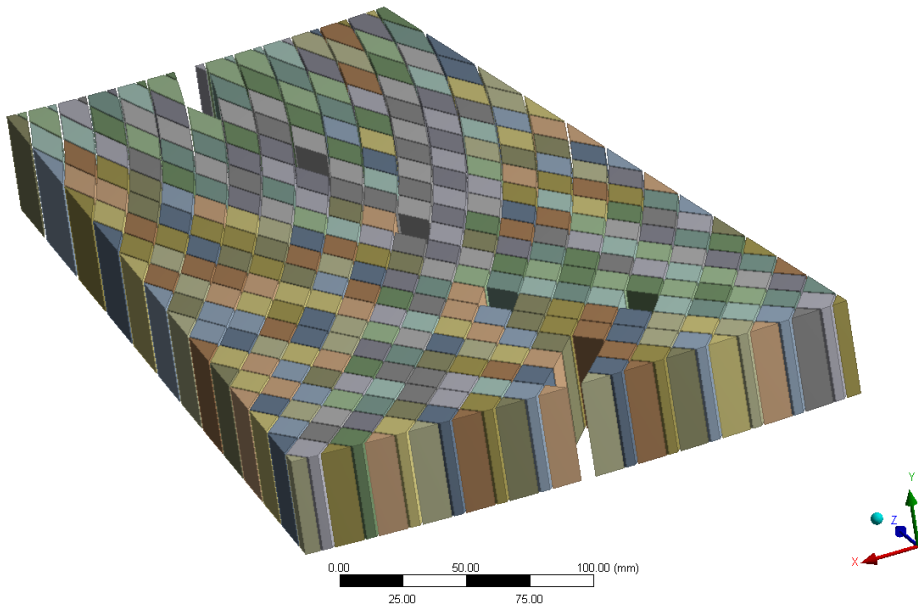


Figure 40. Location of the modeled grains with respect to the target sector

Figure 41 shows the peak equivalent Von Mises stress in some of the grains along the middle line of the target sector. Since the heat is more uniformly distributed in this model the peak stresses appear lower. Note that the edges of the grains used for this model were filleted with a radius of 2mm.

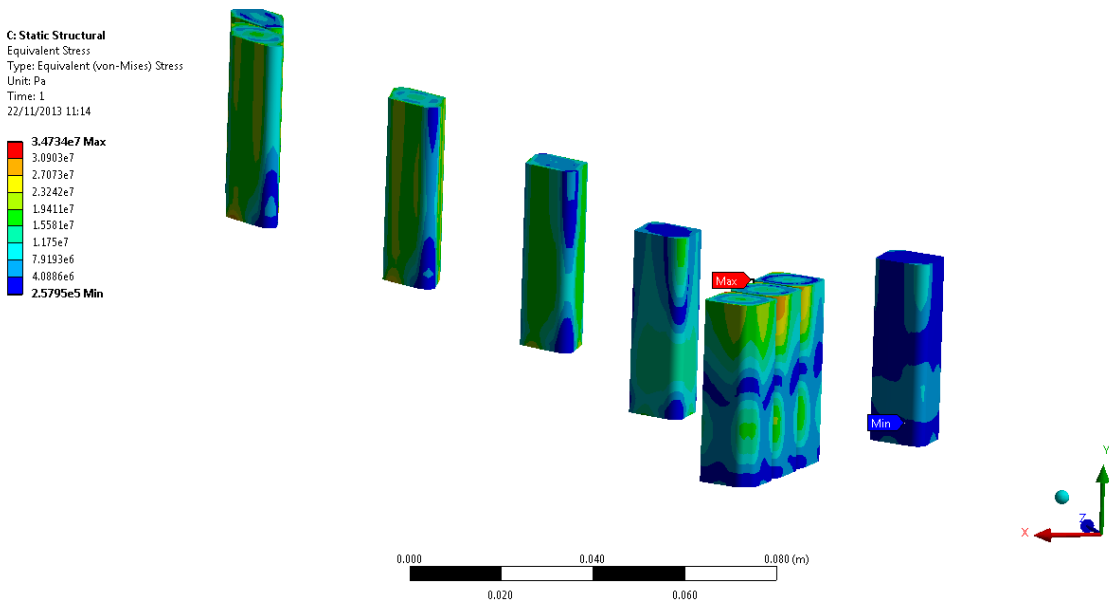


Figure 41. Equivalent Von Mises stress arising from "steady state" heating of the grains. Middle plane section on top of the grains

The total deformation of the grains appears to be small of the order of 25  $\mu\text{m}$  as shown in Figure 42.

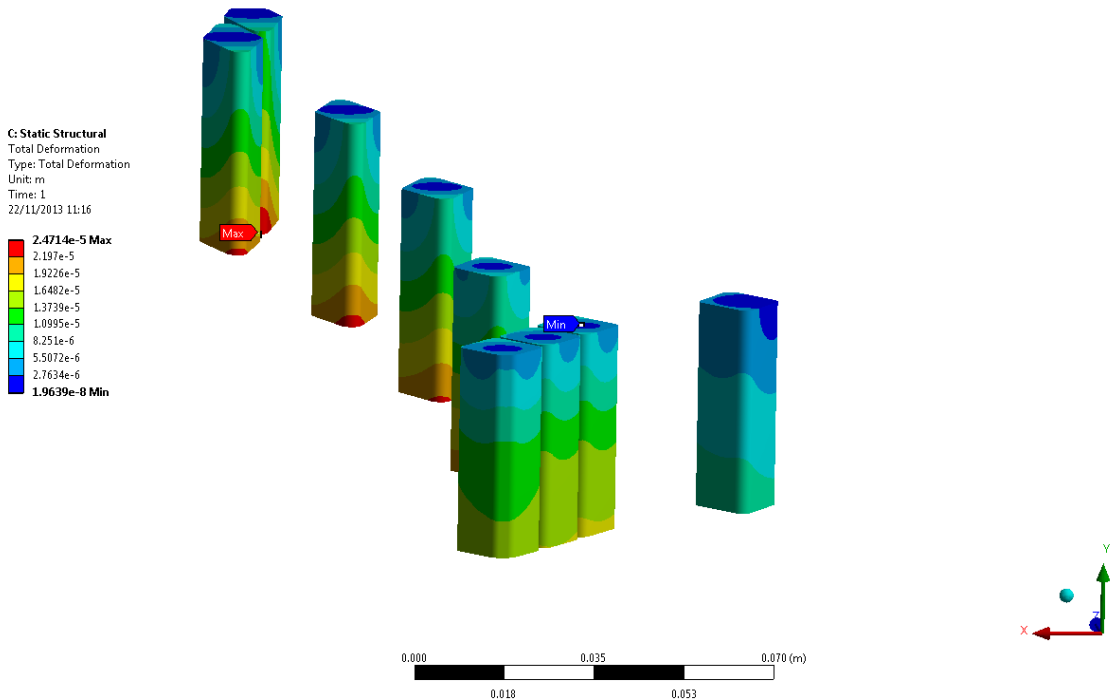


Figure 42. Total deformation in the grains arising from "steady state" heating. Middle section plane on top of the grains

## 2.5 Discussion

This study shows that segmentation of the target is effective in both reducing the peak stresses and peak temperatures in the material. Segmentation to a characteristic dimension around 10 mm appears appropriate to bring the peak stresses well below 100MPa. However, the shape and characteristic dimension of the grains should be object of further investigation as small variations in the characteristic dimension result in sizeable variation on both the complexity of the target and the peak stresses. A regular segmentation pattern, such as the one presented here has the advantage of maximising the overall material packing fraction (86%v/v for the example here presented) whilst also minimising the pressure drop of the cooling gas. On the downside, this type of patterned segmentation produces grains of different shape which require careful production and assembly.

A fully optimised solution is likely to indicate that only the part of the target subject to high beam energy deposition requires segmentation and so the rear end of the target could be made up of blocks or plates reducing the complexity and number of parts in the wheel.

For a non-rastered, full size beam footprint, a uniformly segmented target such as the one shown in Figure 33 could be rotated slowly with consecutive beam footprints overlapping to produce a nearly uniform peak temperature. Synchronisation with the beam pulses would not be necessary and this would avoid the complexity of raster scanning the beam. The peak operating temperatures and stresses would be significantly reduced (to approximately half) and also radiation damage of the material is likely to be better distributed. Ultimately this could increase the life time and reliability of the target.

## 2.6 Modular design

Since reliability of an assembly decreases with the power of the number of constituent elements, a way to increasing reliability could be to separate the wheel into 33 self-contained and individually replaceable target cartridges and to retain the synchronisation of the beam pulses with the target rotation. This modular design could allow isolation of a damaged target cartridge until a scheduled maintenance shut down. In the event of premature failure a target cartridge could be remotely withdrawn and replaced hence reducing operational downtime.

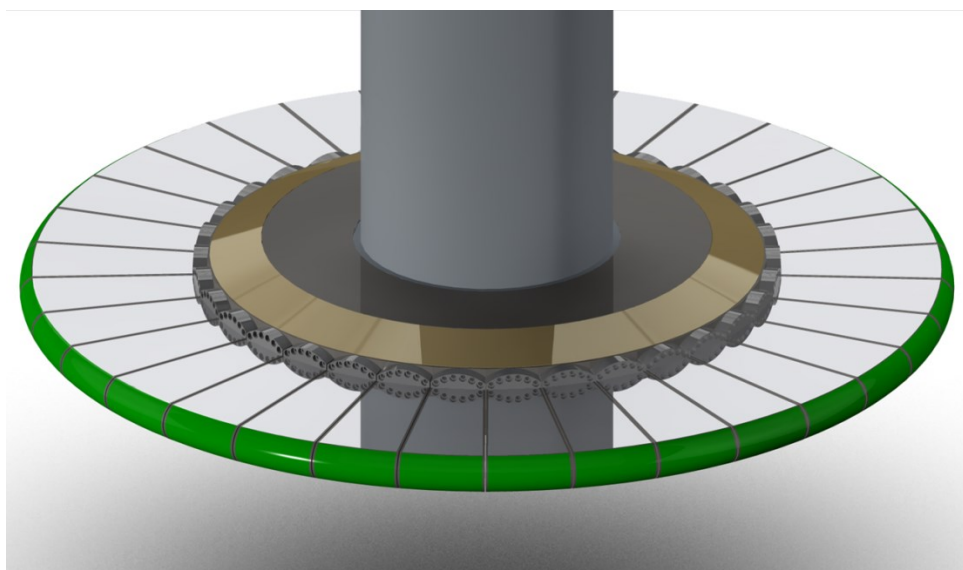


Figure 43. Target wheel modular design concept

A sketch of the modular design concept is presented in Figure 43 which shows the complete target wheel with 33 target cartridges.

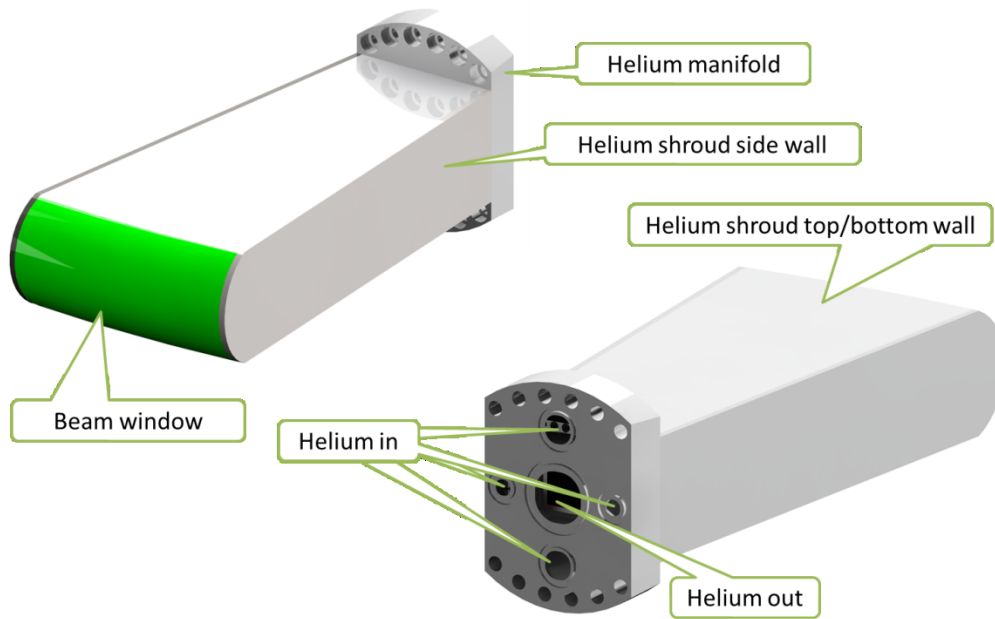


Figure 44. Modular design concept. Stand-alone target section

Figure 44 shows one stand-alone target cartridge. Here the beam window is highlighted in green. The rear support flange of the module also acts as a manifold incorporating the supply and return channels for the helium coolant. From the flange the four supply channels enter a series of holes drilled in the top, bottom and side walls of the shroud. This makes the vessel material more transparent to the emitted neutrons yet stiffer.

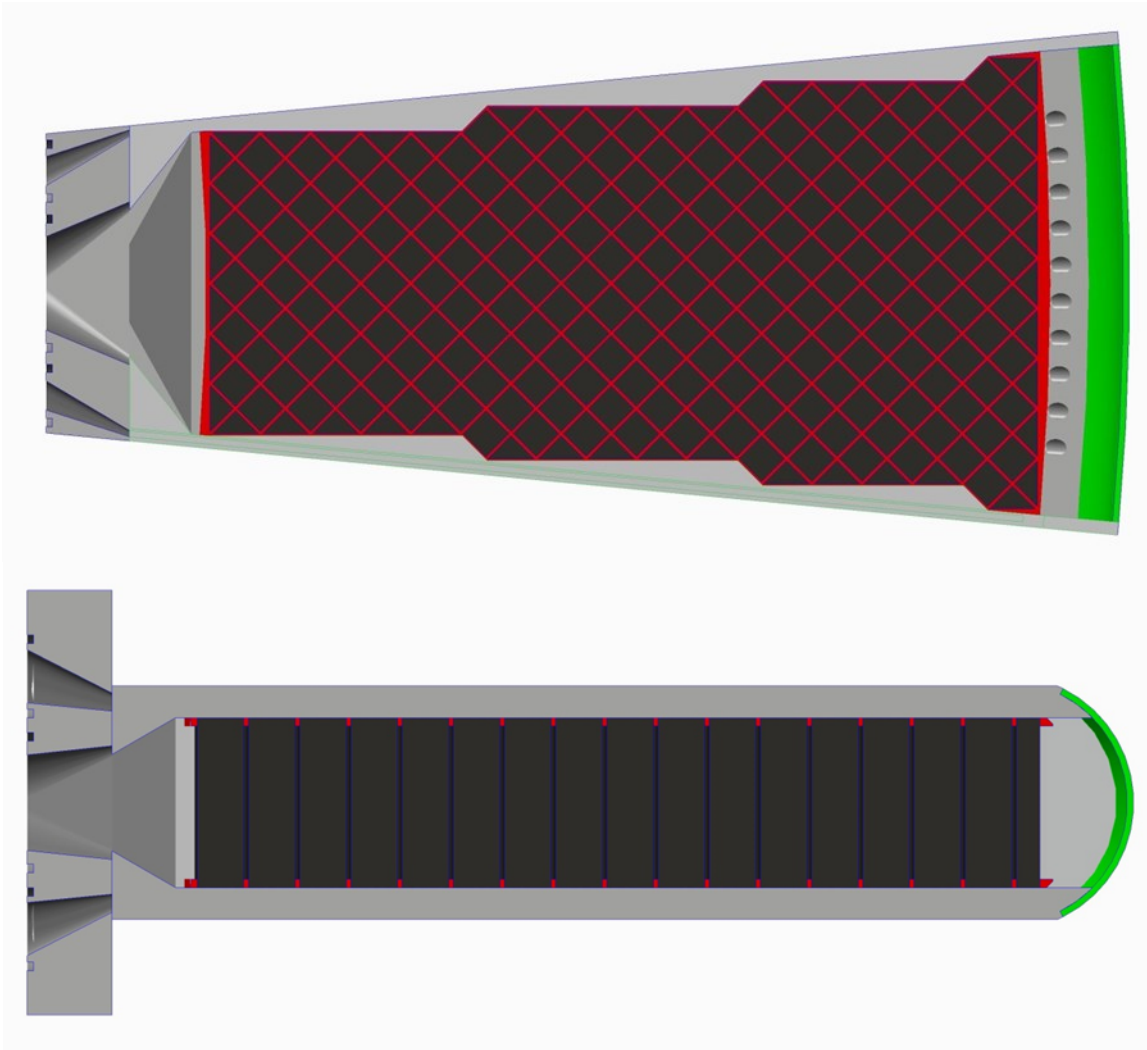


Figure 45. Horizontal and vertical sections of one stand-alone target cartridge

Figure 45 shows a horizontal and vertical section of one cartridge with the tungsten grains in black. The red matrix locating the grains could be either machined into the top and bottom plates or be a separate component. A set of helium supply channels (a series of small holes) cooling the front window is visible on the right on the top section in Figure 45.

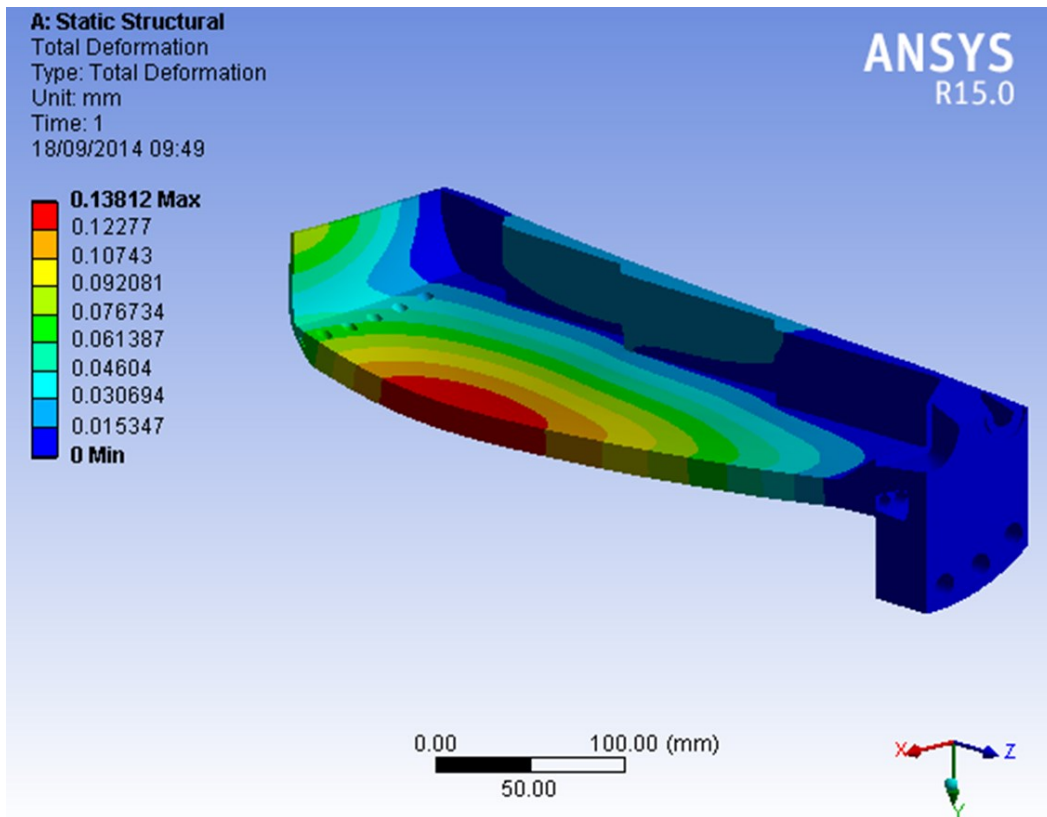


Figure 46. Deformation of the shroud and beam window under coolant pressure

The simulation in Figure 46 reports small deformations in the bottom shroud and window when subjected to 3 bar helium pressure. Note that with this design the beam entry window becomes smaller, stiffer and integral to each individual target cartridge and therefore not crucial to the life span of the whole target wheel assembly.

Cross sections comparing the assembly of modular design concept with the original baseline design are reported in Figure 47 and Figure 48.

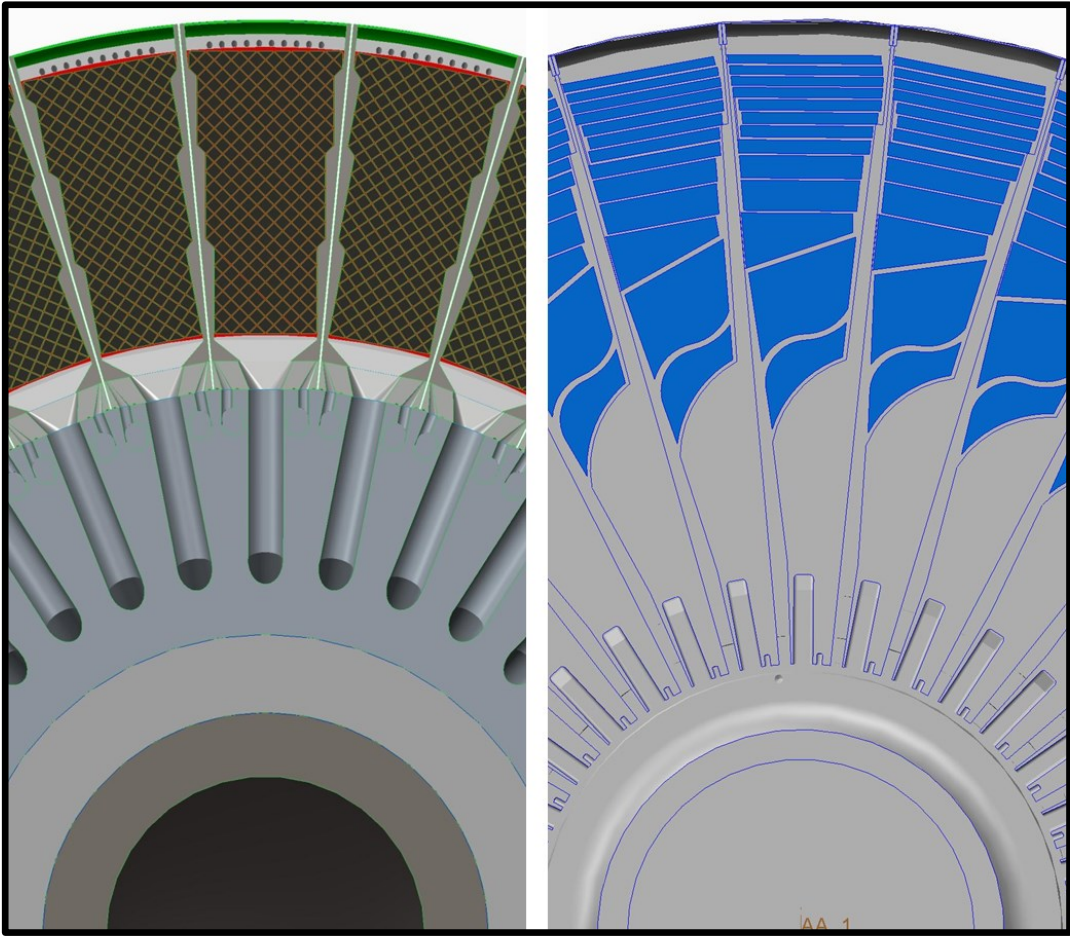


Figure 47. Horizontal cross section comparison between the modular design concept (left) and baseline design (right)

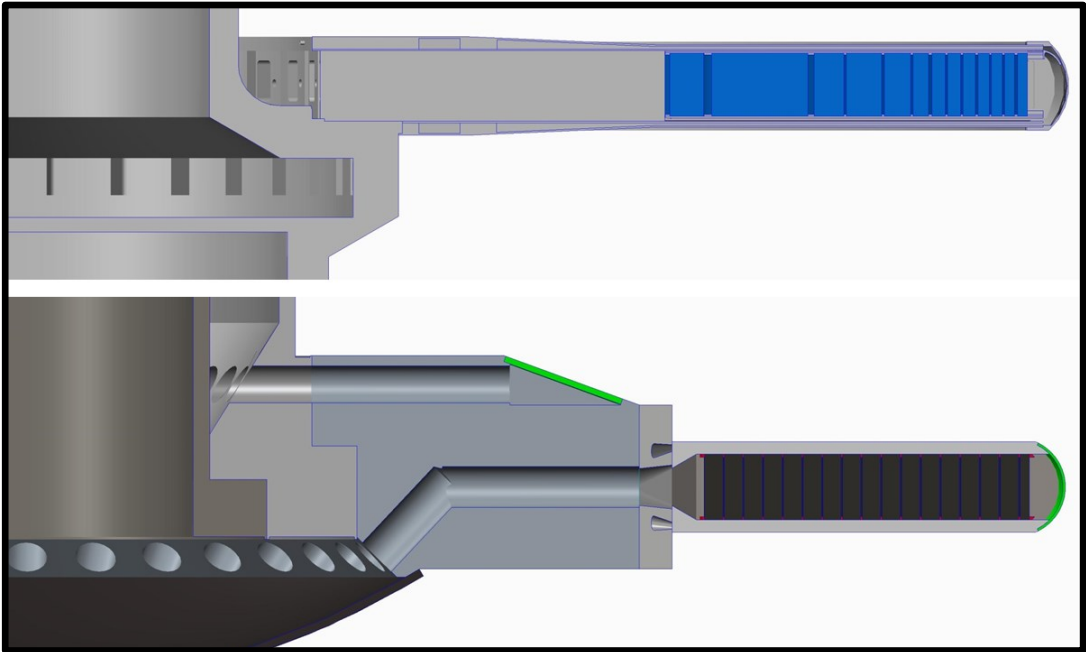


Figure 48. Vertical cross section comparison between the modular design concept (bottom) and baseline design (top)

### 3 Helium gas circulation energy considerations

Circulating the required 3kg/s of helium gas with a pressure drop of 1bar or more requires a significant amount of energy. There are several options available to achieve the helium flow and the final selection may have a significant bearing on the energy consumption of the helium circulation unit. The ideal compression power of the gas can be calculated from the following expression which is easily obtained from the Steady Flow Energy Equation.

$$W_c = \dot{m}C_pT_{01} \left( \frac{P_{02}}{P_{01}}^{\frac{\gamma-1}{\gamma}} - 1 \right)$$

where m represents the mass flow through the compressor,  $C_p$  is the heat capacity of the gas (5200J/kgK for helium),  $\lambda$  is the ratio of specific heats for the gas (1.66 for helium), T and P represent temperature and pressure with index 1 referring to compressor inlet condition and index 2 referring to compressor outlet conditions.  $W_c$  represents the work done on the gas to isentropically compress it from state 1 to state 2. A real compressor will not achieve isentropic compression and will also have mechanical losses. Accounting for isentropic and mechanical efficiencies then actual compressor power will be typically of the order of 1.3 to 1.4 times larger than the ideal compression power.

An important decision which affects the power consumption of the helium compressor is the operating pressure in the circuit. This design decision also has significant bearing on the structural design of the target as well as the neutronics performance.

If we assume the helium circuit will have a total pressure drop of 1bar independent of the operating pressure (this is based on preliminary concept designs of the target wheel) then we can see from the ideal compression power expression that as operating pressure increases the pressure ratio reduces and compression power is consequently reduced (Figure 49).

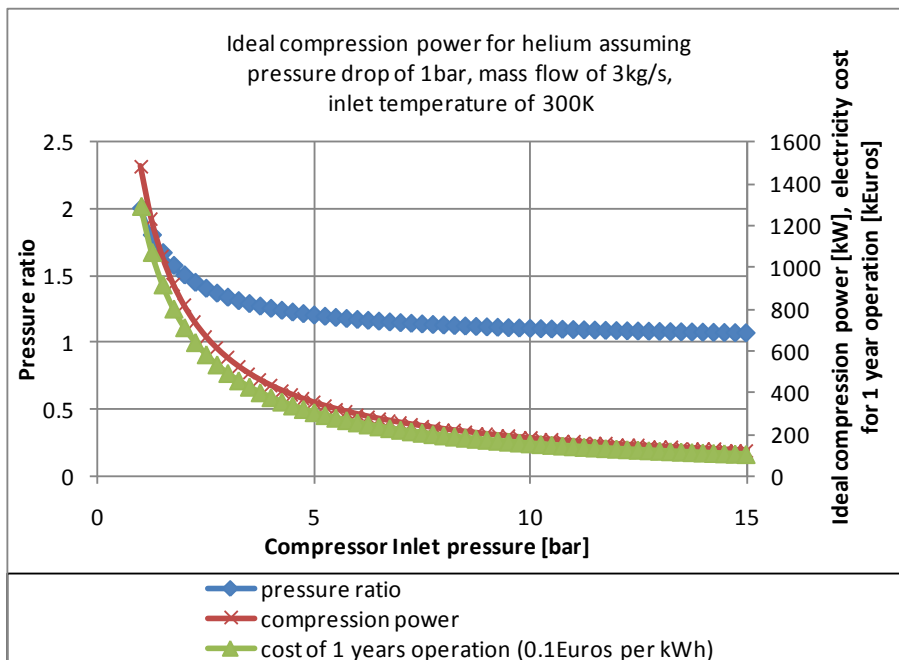


Figure 49 Ideal power consumption of helium compressor

### 3.1 A multistage centrifugal fan type compressor

Following communications between RAL and Dresser a multistage centrifugal compressor was proposed by Dresser (Figure 50, Figure 51) as being the most appropriate machine to provide the demanding helium flow rate and pressure ratio requirements. The table below shows three options that they propose. There is a clear requirement from the design of the target wheel to keep pressure to a minimum however it was clear from the point of view of the compressor that a higher pressure machine would be easier to build, cheaper to run and less stressed. The lowest discharge pressure Dresser proposed was 4bar. Providing the required mass flow at lower pressures was not seen as possible within their existing design strategies. The knowledge that option 1 is a possibility is driving the design of the ESS target wheel. Complete speed curves for the three options are available in Appendix 4.1. The options put forward by Dresser are based on a helium mass flow of 3kg/s and a helium inlet temperature of 300K.

Option	Inlet pressure	Outlet Pressure	Number of Stages	Shaft Power	Shaft Speed	Outlet Temp
1	3bar	4bar	4	807kW	11710rpm	350K
2	5bar	6bar	3	491kW	11392rpm	330K
3	9bar	10bar	4	279kW	7422rpm	317K

The main application for these multi stage centrifugal compressors is pumping large amounts of natural gas. The compressors are well proven with much industrial experience of minimal maintenance long term operation with a range of gases including corrosive gases. Various materials are possible for construction of the impellers and casings. Crane 28 double seals are recommended for sealing helium. Some more head room is available on pressure ratio by increasing to 7 stages or running faster although the latter does incur a complexity and reliability penalty. They typically make a sound level of 90dBa without acoustic box. They can be powered by electric motor or steam turbine.

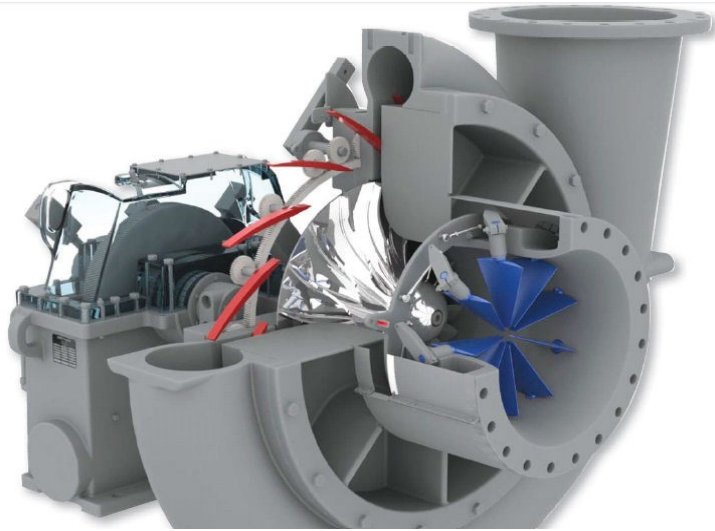


Figure 50 Dresser centrifugal compressor

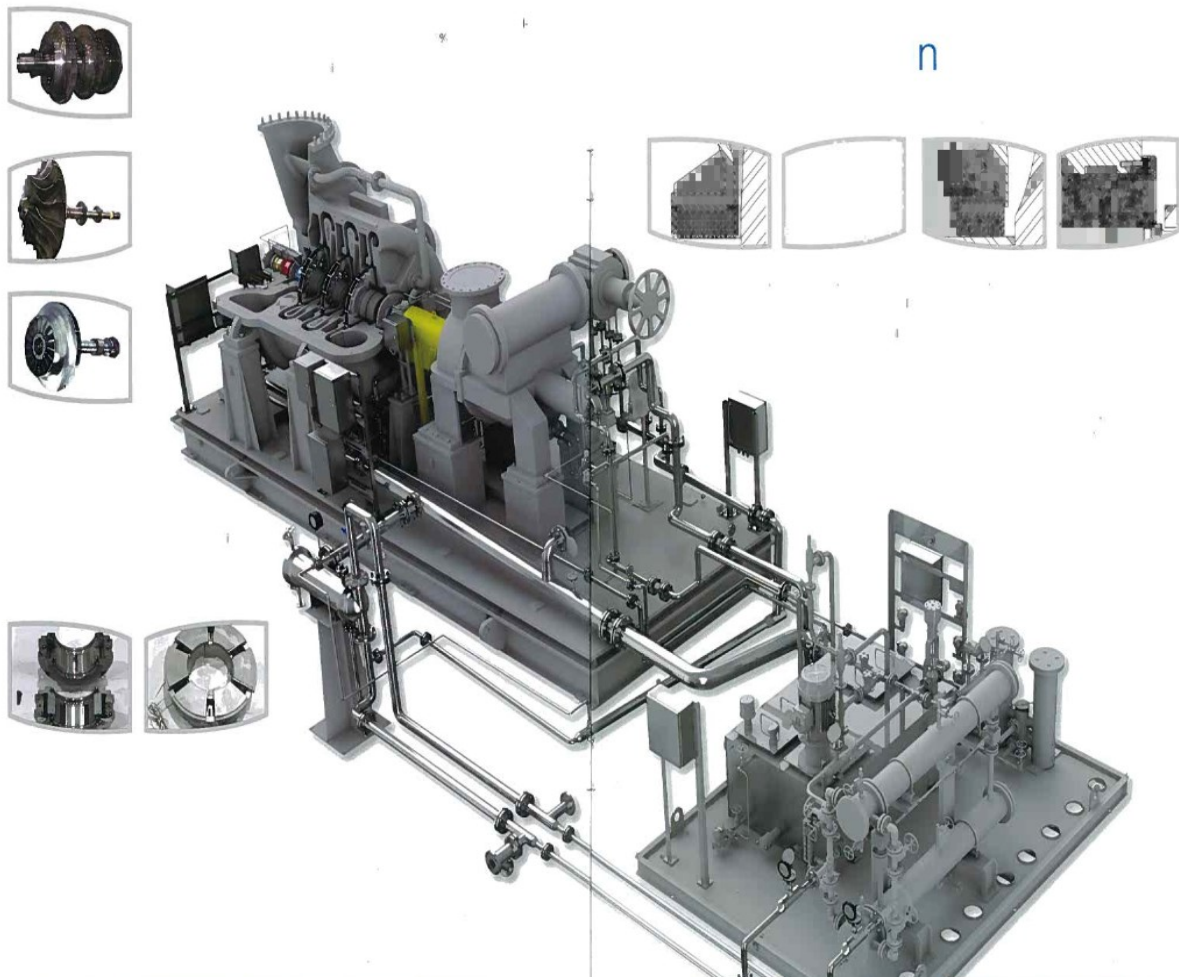
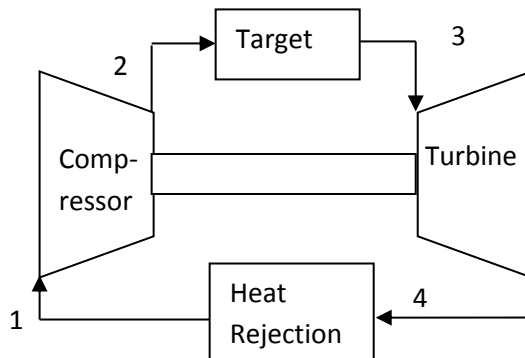


Figure 51 Multistage centrifugal compressor

### 3.2 A closed cycle brayton cycle

One alternative to an electric motor powered compressor which is of interest from an energy saving point of view is to design a closed cycle helium gas turbine plant, similar to what has been developed in the past for advanced gas cooled reactors. Helium would be compressed by a multistage axial compressor, this gas would then enter the target where 3MW of heat power are added to the helium as it passes over the spallation material. The heated pressurised gas would then expand through a multi stage axial turbine which would drive the compressor through a shaft. The remaining heat in the turbine exhaust could be used to heat water. Below is a simple diagram of the circuit.



Assume pressure drop in target and surrounding pipework is 0.5bar and pressure drop in heat rejection heat exchanger and surrounding pipe work is also 0.5bar. Take mass flow to be 3kg/s,  $P_{01}=1\text{bar}$  and  $T_{01}=300\text{K}$ . Assume isentropic compression and expansion from 1-2 and 3-4 respectively. Assume 3MW of heat addition between 2 and 3.

Without taking in to account mechanical and isentropic efficiencies a simple analysis shows that a compressor pressure ratio of 4.8 : 1 would be required. This gives enough pressure to cover the assumed 1bar pressure drop in the target and heat exchanger and results in a high enough turbine inlet temperature and turbine pressure ratio such that the turbine can power the compressor. The temperatures and pressures at each point in this example ideal circuit are shown in the table below. Higher turbine inlet temperatures would be desirable to make turbine blade design simpler. As such a lower mass flow rate through the target enabling the helium to get hotter may be desirable.

circuit absolute stagnation pressures bar	$P_{01}$	$P_{02}$	$P_{03}$	$P_{04}$
	1	4.8	4.3	1.5
circuit absolute stagnation temperature K	$T_{01}$	$T_{02}$	$T_{03}$	$T_{04}$
	300	560	760	500
compression power [Watts]	$w_{12}$	4051740		
turbine power [Watts]	$w_{34}$	4054636		

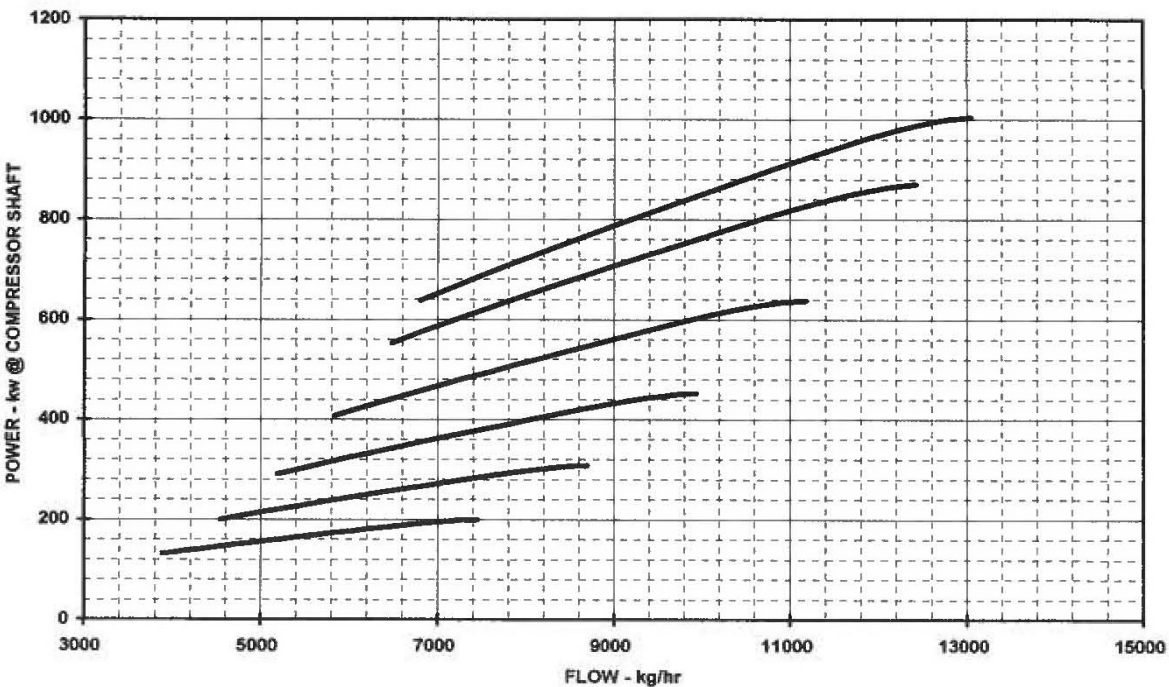
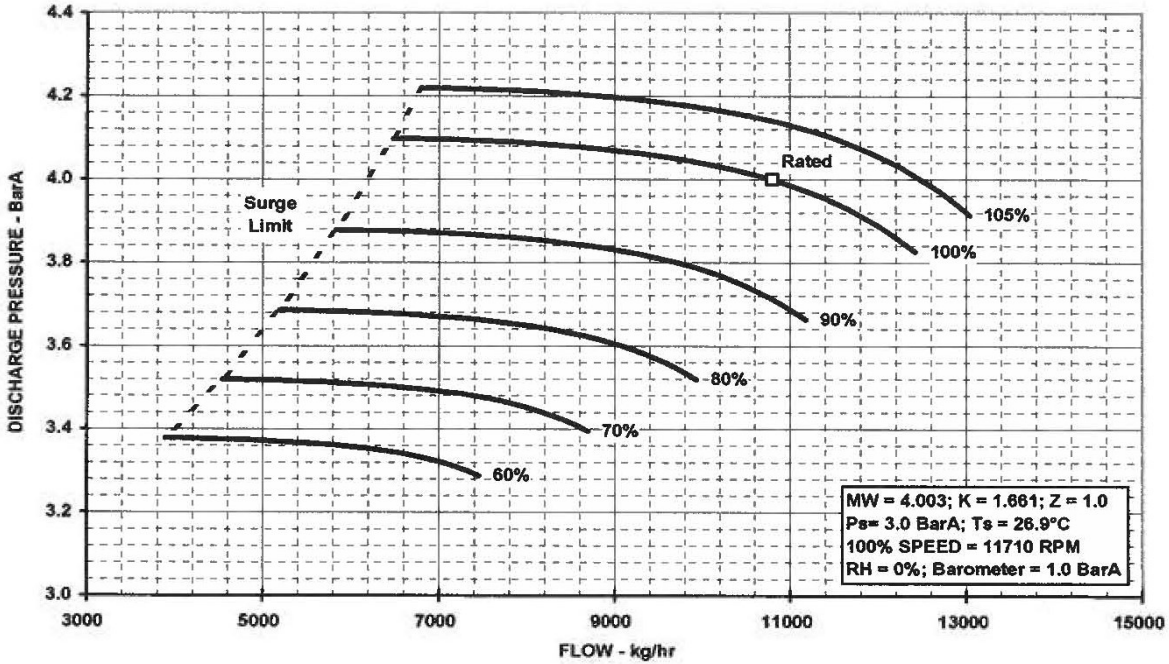
## 4 Appendices

### 4.1 Appendix: Predicted performance of Dresser multistage centrifugal compressor

Calculated Performance  
for Roots HN-194  
with Variable Speed

**Rutherford**  
Helium Blower  
Option # 1

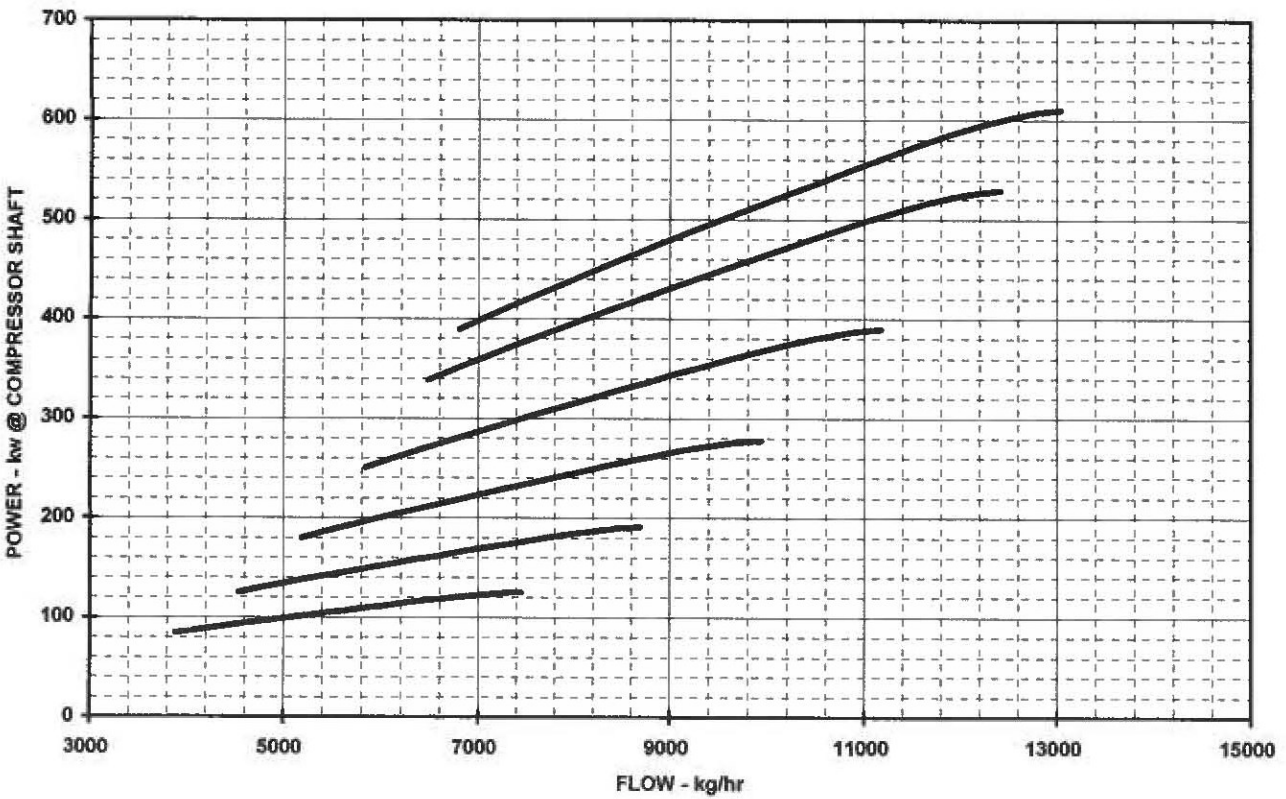
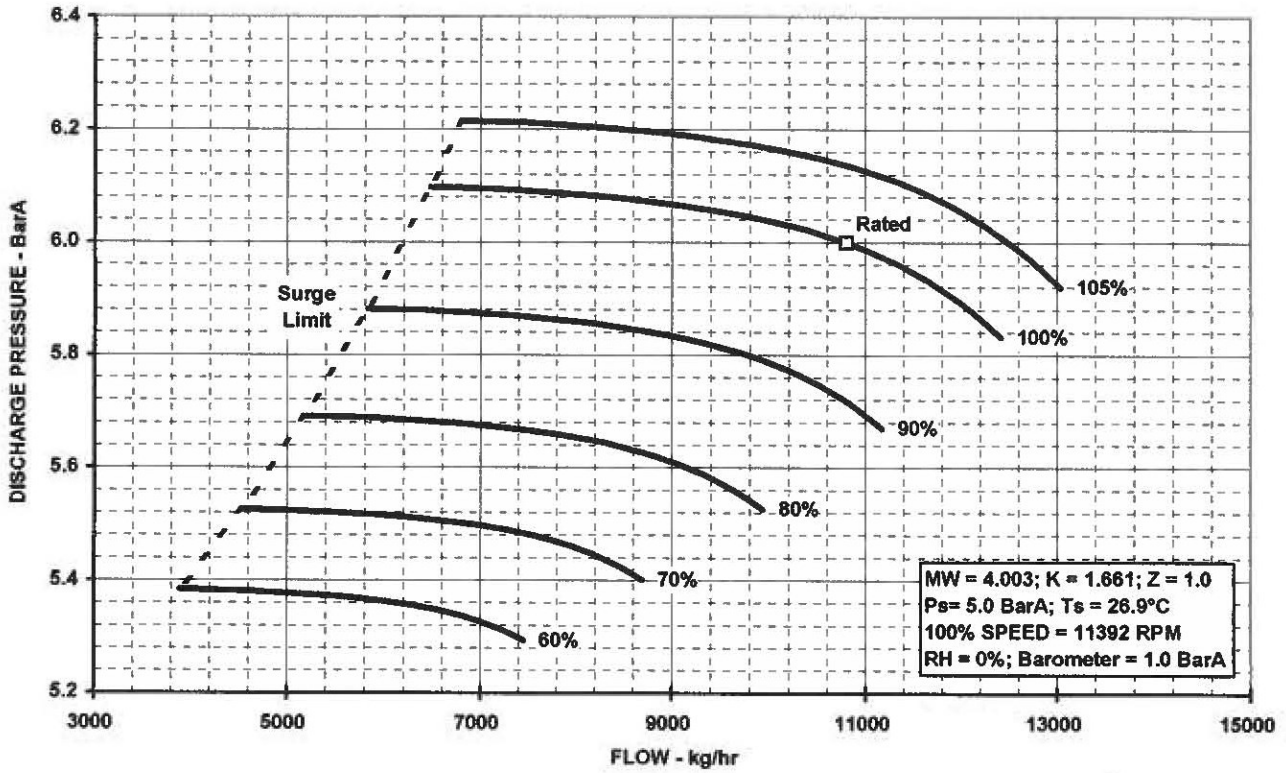
Pressure and Power  
vs Flow



Calculated Performance  
for Roots HN-193  
with Variable Speed

**Rutherford**  
Helium Blower  
Option # 2

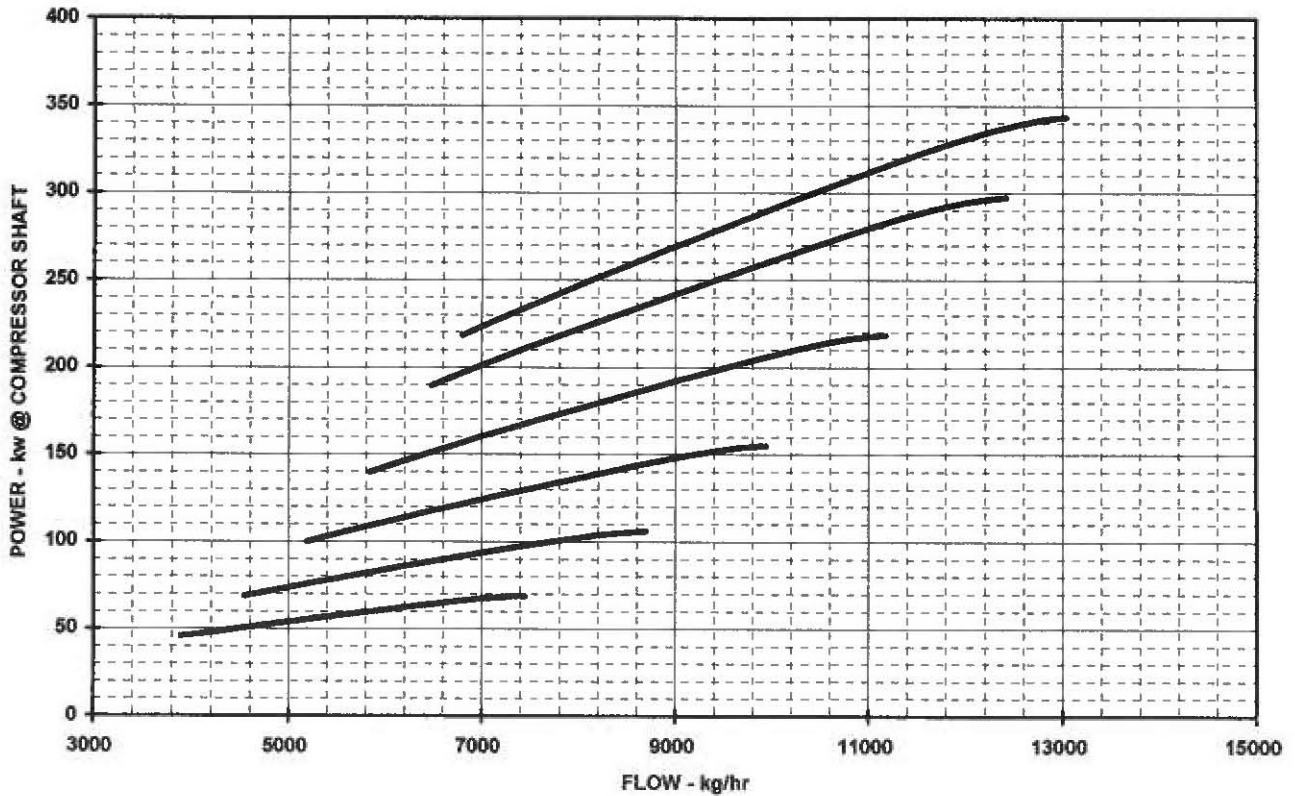
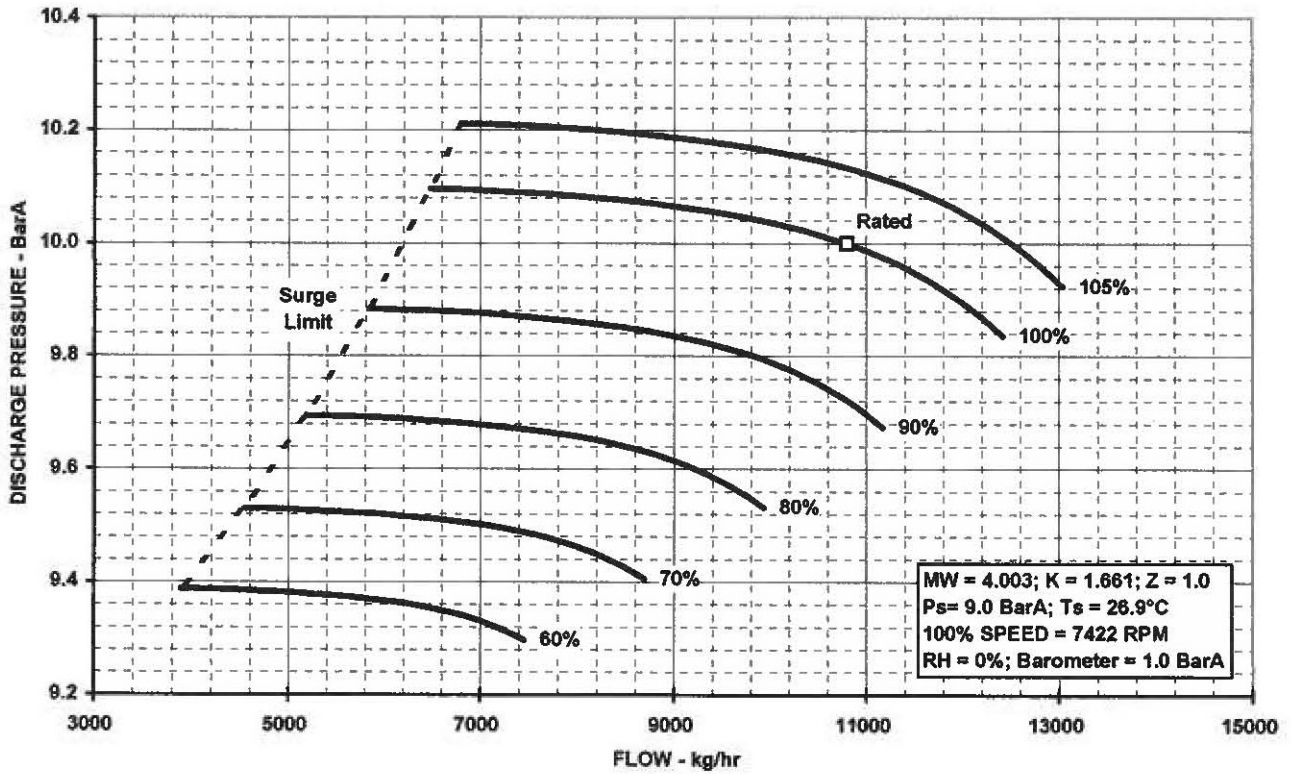
Pressure and Power  
vs Flow



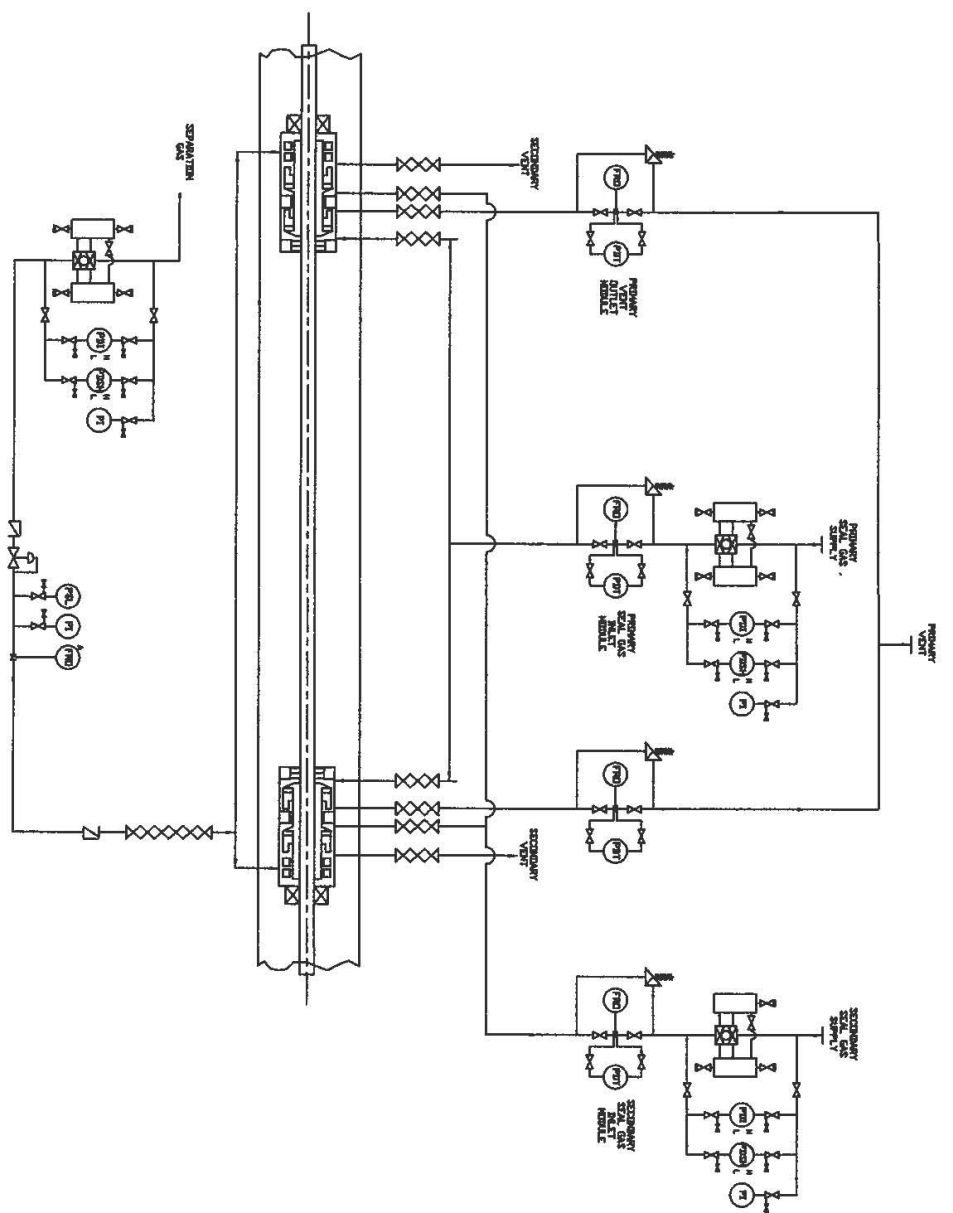
Calculated Performance  
for Roots HN-194  
with Variable Speed

**Rutherford**  
Helium Blower  
Option # 3

Pressure and Power  
vs Flow



*Handwritten signature*



REV.	REVISIONS	DATE

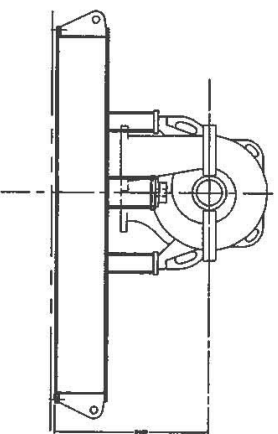
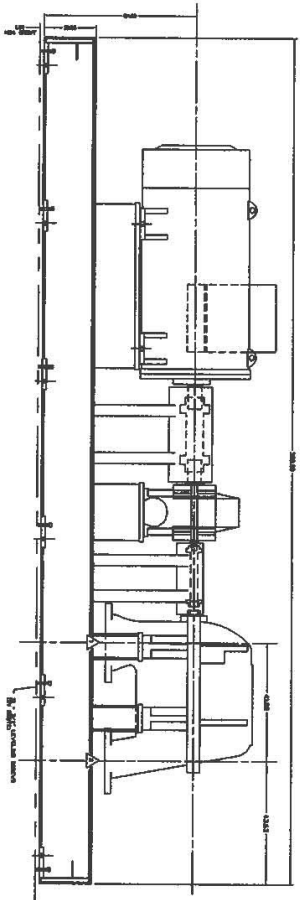
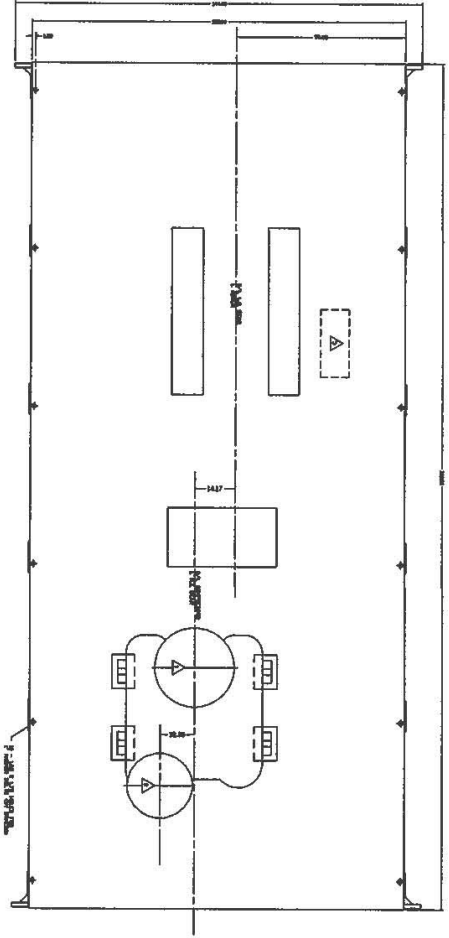
- ⊗ XX GAUGE BOARD MOUNTED INSTRUMENT.
- ⊗ XX X LOCALLY MOUNTED INSTRUMENT.
- ⊥ RETURN LINE TO RESERVOIR.
- ⇨ OTHER LIMITS OF SCOPE OF SUPPLY.

THIS IS A VISUAL REFERENCE DRAWING ONLY. DIMENSIONS & FLOW DIRECTION MAY BE CHANGED BY LUBER-PWR, INC. BASED ON THE CUSTOMER'S ACTUAL SPECIFICATIONS AND/OR MODIFIED OPTIONS. DO NOT DESIGN ANY EQUIPMENT BASED ON THIS DRAWING.

THIS DRAWING INCLUDES CONFIDENTIAL INFORMATION WHICH IS THE PROPERTY OF LUBE-POWER, INC. THIS COPY IS LOANED FOR A SPECIFIC PURPOSE. WITH THE UNDERSTANDING THAT IT WILL NOT BE REPRODUCED, USED FOR ANY OTHER PURPOSE OR DISCLOSED TO OTHERS WITHOUT WRITTEN CONSENT OF LUBE-POWER, INC.

LUBE-POWER, INC. SHELVY TOWNSHIP, INDIANAPOLIS, IN  
 (317) 547-6500  
 (317) 547-6500  
 FAX (317) 547-6500

DATE: 05/27/20 SCALE: NONE DRAWN BY: M.R.B.  
 PRELIMINARY PIPING & INSTRUMENTATION DIAGRAM  
 CUSTOMER: DRESSER-ROOTS DRAWING NO.: 9800-ROOTS



PRELIMINARY ONLY  
NOT FOR CONSTRUCTION

CUSTOMER CONNECTIONS	
<b>A</b>	COMPRESSION INLET FLANGE 18 INCH I.D. (NOMINAL) 1800 S.S. 25 BNC
<b>A</b>	DISCHARGE 18 INCH I.D. (NOMINAL) 1800 S.S. 25 BNC
<b>A</b>	1" HOLES IN BASE FLANGE STAINLESS STEEL (NOMINAL) 18 INCH I.D. 18.75 BNC
<b>A</b>	MOTOR CONNECTION BOX CONNECTION (LOCATION TBD)

APPROXIMATE WEIGHTS IN LBS.	
COMPRESSOR	12,400
MOTOR	12,700
BASE	4,000
ACCESSORY & AUXILIARIES	52,817
TOTAL WEIGHT	56,117
WEAREST LIFT BEYOND INSTALLATION	56,117
WEAREST LIFT WITH FOUNDATION	56,117

- NOTES:
- 1) 1.50" MINIMUM CLEAR UNDER THE BASEPATE WITH THE MASTRAC.
  - 2) ANY PIPING CONNECTED TO GROSS COMPRESSION FLANGES MUST BE PROPERLY SUPPORTED.
  - 3) CONNECTIONS IN THE FOUNDATION PAD EXTENDS MINIMUM 18.00" OUT FROM THE FOUNDATION PAD.
  - 4) COMPRESSOR SECTION AND DISCHARGE PIPING.

THIS DOCUMENT CONTAINS CONFIDENTIAL INFORMATION OF ROOTS. IT IS TO BE KEPT STRICTLY CONFIDENTIAL AND NOT TO BE DISCLOSED TO ANY OTHER PERSON OR ORGANIZATION WITHOUT THE WRITTEN PERMISSION OF ROOTS.

**SHIPPING AND DATA CERTIFIED**

PACKAGE ORDER NO. \_\_\_\_\_

EQUIPMENT NO. \_\_\_\_\_

ROOTS ORDER NO. \_\_\_\_\_

DATE \_\_\_\_\_

**GENERAL ARRANGEMENT**

RR-905 CENTRIFUGAL COMPRESSOR

**Roots**

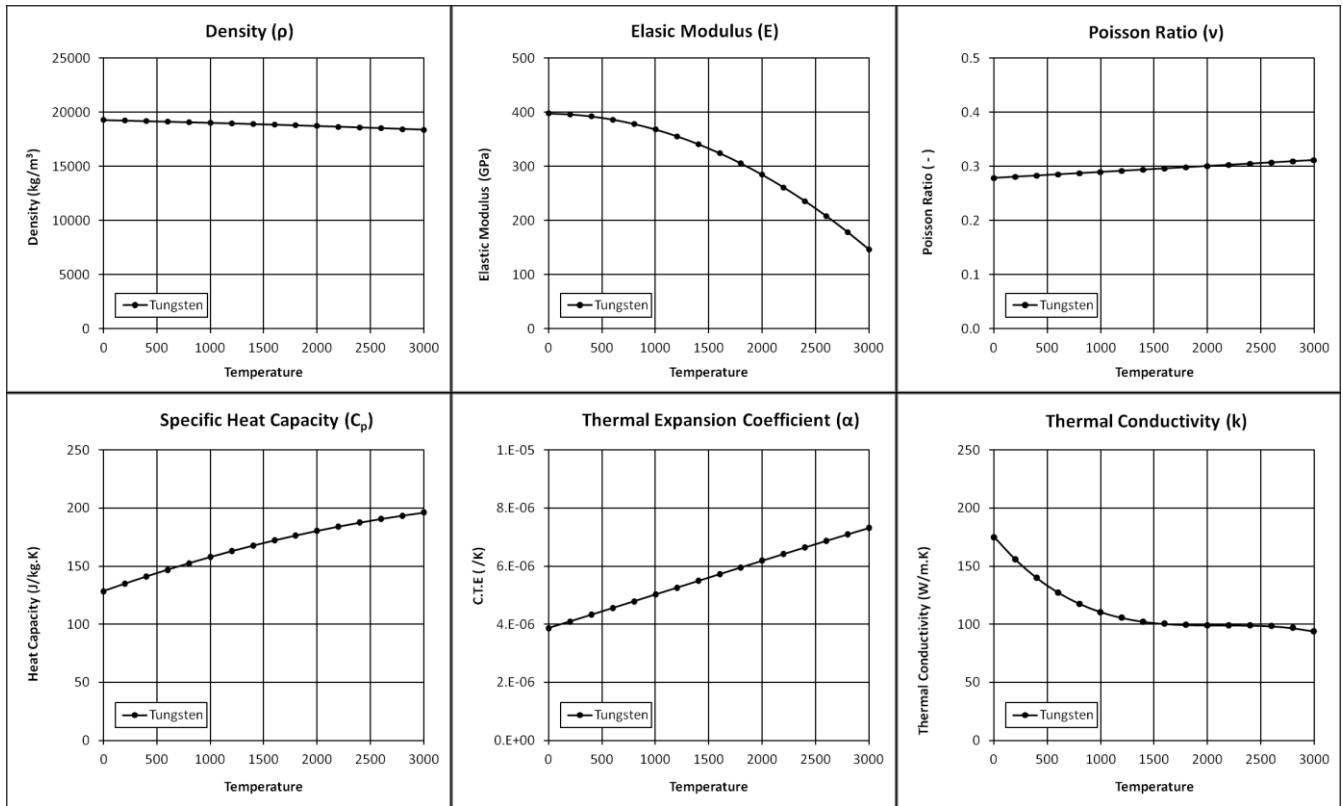
Roots Blower Corp., Inc.

SHRDL-10000-P3-CM REV. A

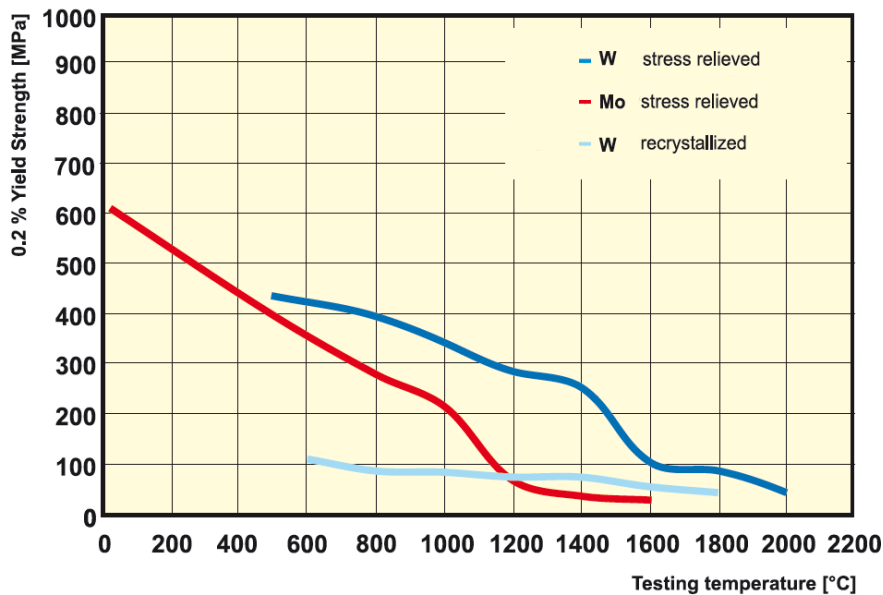
SHEET 1 OF 3

11 12 13 14 15 16 17 18 19 20 21 22 23 24 25 26 27 28 29 30 31 32 33 34 35 36 37 38 39 40 41 42 43 44 45 46 47 48 49 50 51 52 53 54 55 56 57 58 59 60 61 62 63 64 65 66 67 68 69 70 71 72 73 74 75 76 77 78 79 80 81 82 83 84 85 86 87 88 89 90 91 92 93 94 95 96 97 98 99 100

## 4.2 Appendix 1 Tungsten material properties

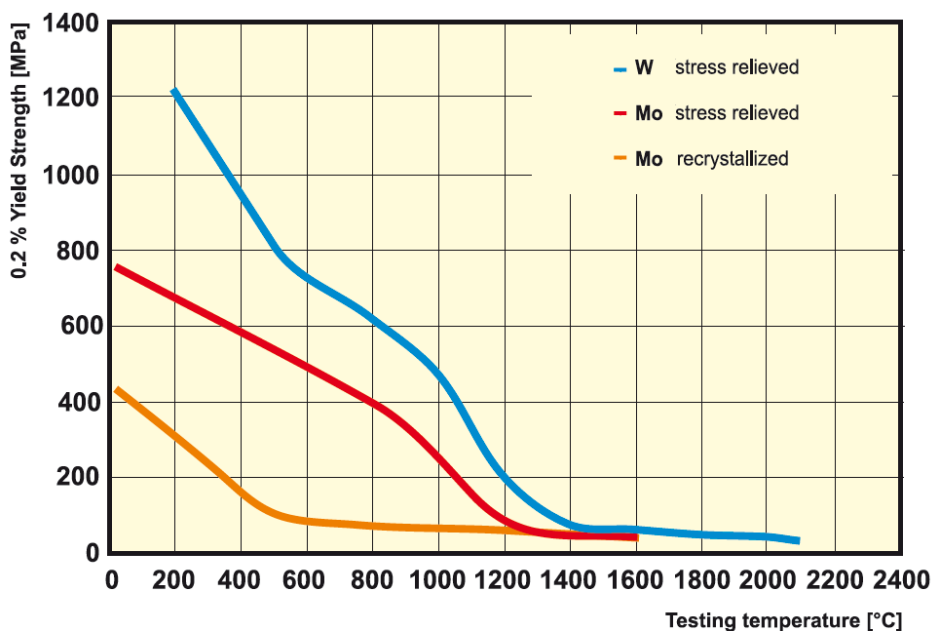


### 4.3 Appendix: tungsten yield strength data as published by Plansee



Typical 0.2 % yield strength for W and Mo rod material in the stress relieved and recrystallized condition respectively (diameter 25 mm)

Figure 52. Tungsten yield strength data for rod



Typical 0.2 % yield strength for W and Mo sheet material in the stress relieved and recrystallized condition respectively (thickness of the sheet: W = 1 mm / Mo = 2 mm)

Figure 53. Tungsten yield strength data for sheet material

#### 4.4 Appendix: sensitivity of the thermal analysis to grains swelling

A simple model was developed to validate the ability of CFX to model the thermal and fluid dynamic conditions used for the simulations in the report. In the model a single helium channel was studied of length 400mm, height 80mm and width 2mm. The long side walls of the channels were loaded with a constant heat flux input of 10kW. The helium flow through the channel was driven by a constant pressure difference of 0.5bar (with a reference pressure of 3.5bar) as would be the case if the helium was fed and returned to a common manifold, rather than by mass flow.

Figure 54 shows the temperature of the side wall increasing along its length as the helium retrieves heat and warms up (in the same fashion as the wall).

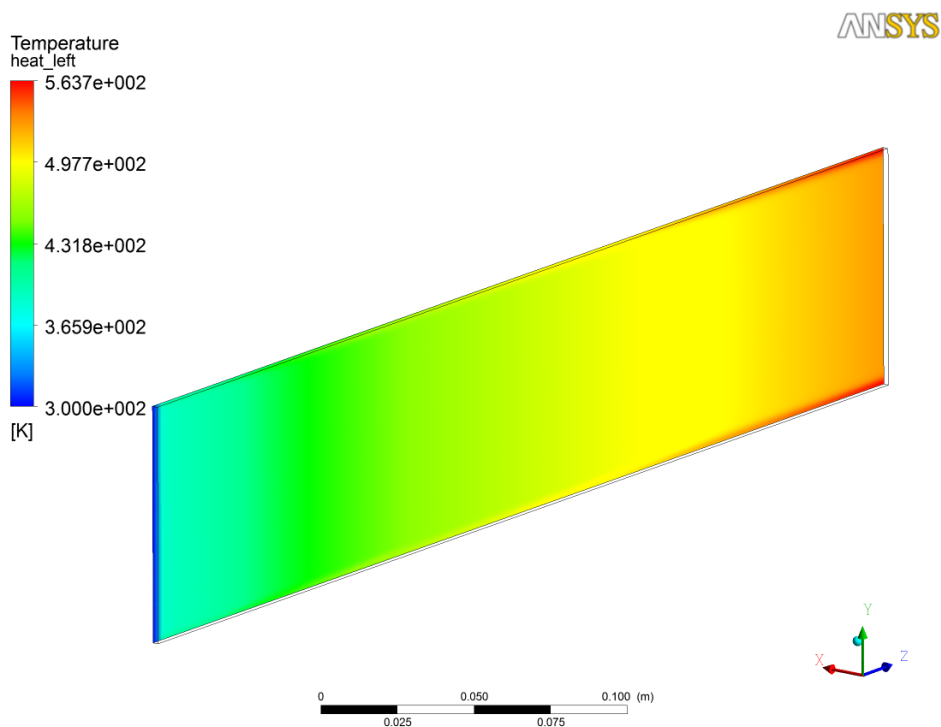


Figure 54. Temperature along the length of the channel wall

Figure 55 shows velocity vectors in the helium stream. Note that the helium speeds up as it heats and expands.

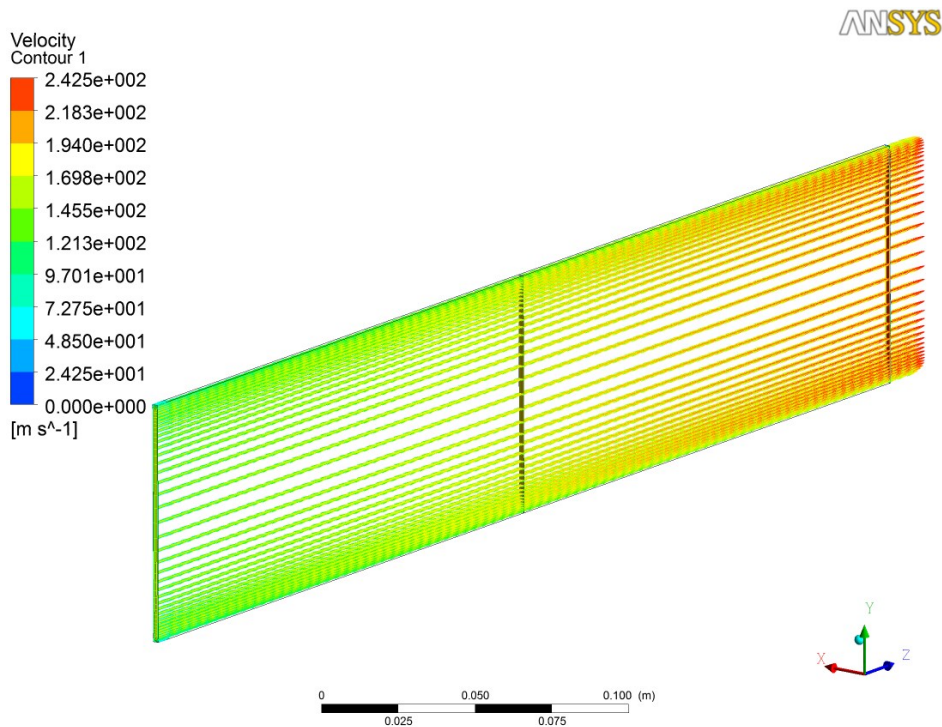


Figure 55. Helium velocity profile along the channel

Simulations parameters are believed to be reasonably representative of a channel along the beam line in the grained target. Whilst CFX models with reasonable accuracy the fluid dynamic properties helium, it is questionable whether the target may operate in a region where the thermal expansion of the grains feeds back on the fluid dynamic conditions. In fact the CFX model does not account for the thermal expansion of the grains and relative shrinkage of the helium channels.

In order to investigate this effect the simplified model described above was parameterised to show the result of channel shrinkage on the helium cooling performance. This offers an insight on a plausible dimensional defect in one of the channels or on uneven heating applied to adjacent channels.

Figure 56 shows the effect of channel shrinkage on the thermal capacity of the channel. Note that as the channel size decreases from the initial 2mm width (bottom axis), the mass flow rate of the helium flowing through the channel also decreases (blue dots on the left hand axis) to the detriment of the plate temperature which goes up (red dots on the right hand axis). So a reduction in the channel size of 200µm (i.e. 10% of the 2mm channel) results in a decrease in the helium mass flow rate of 18% and a consequent increase in the plate temperature of 33K.

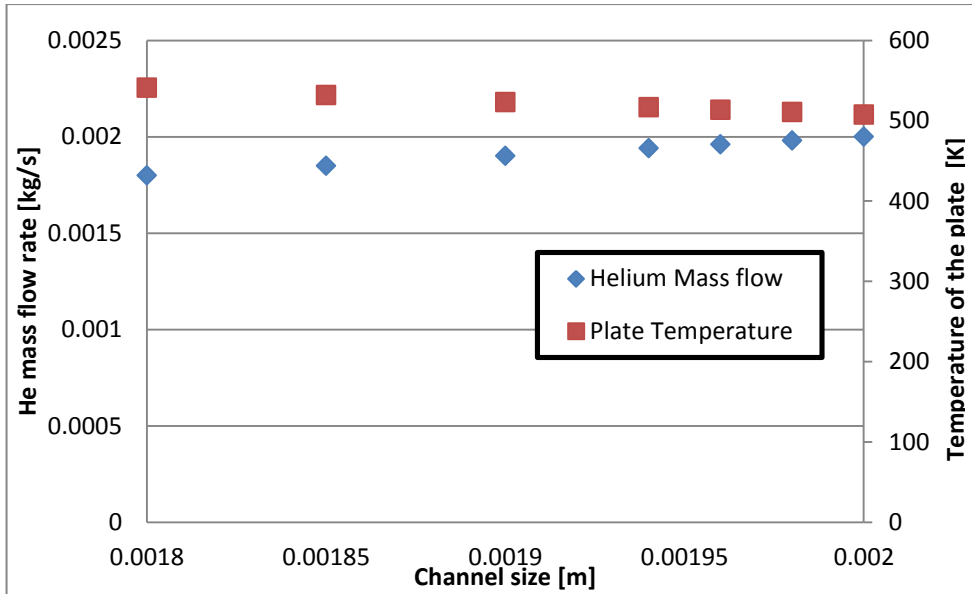


Figure 56. Thermal capacity of channel to channel size

Figure 57 shows the feedback effect relative to the situation described above. Here you can see the thermal expansion of 15mm wide grains as a percentage of the initial 2mm width helium channels. As the temperature of the helium rises from the initial 507K (for a 2mm width channel) due to an unforeseen shrinkage of the helium channel, the grains will thermally expand resulting in an even smaller channel width. As you can see in the Figure however the feedback effect appears negligible as the grains expansion is a rather small fraction of the initial 2mm width channels.

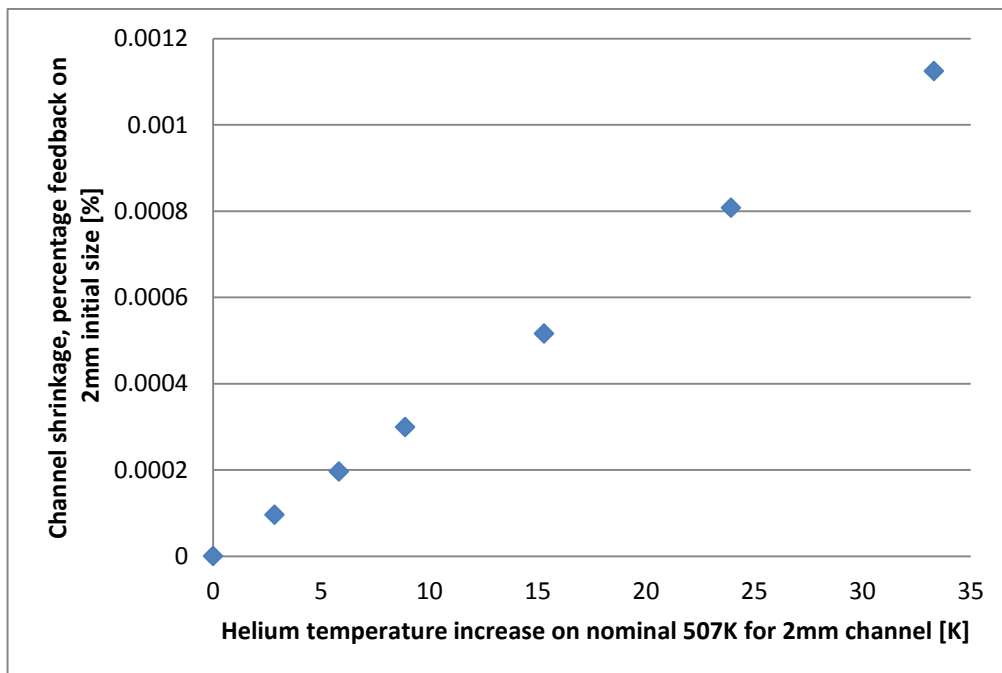


Figure 57. Feedback effect due to thermal expansion of the grains

## 5 References

- [1] ESS Technical Design Report. 2012
- [2] Thermo-mechanical assessment of the ESS helium cooled rotating tungsten wheel design & comments on the helium circulator. 2013. Tristan Davenne
- [3] Plansee brochure. Tungsten Material Properties and Applications. 2012
- [4] H.E. Boyer, 'Atlas of fatigue curves', ASM 1986.
- [5] T.E.Tietz and J.W.Wilson, Behaviour and properties of Refractory metals: Edward Arnold publishers Ltd., 1965.